LBL-15435 c.2

Lawrence Berkeley Laboratory
UNIVERSITY OF CALIFORNIA

Materials & Molecular Research Division

RECEIVED
LAWRENCE
BERKELEY LABORATORY

OCT 19 1983

LIBRARY AND
DOCUMENTS SECTION

MICROSTRUCTURES, TRANSFORMATIONS AND PROPERTIES OF OXIDATION-RESISTANT, IRON-BASE, ALUMINUM-MODIFIED ALLOYS

Gustavo Luis Tamayo
(M.S. Thesis)

December 1982

TWO-WEEK LOAN COPY

This is a Library Circulating Copy which may be borrowed for two weeks. For a personal retention copy, call Tech. Info. Division, Ext. 6782.

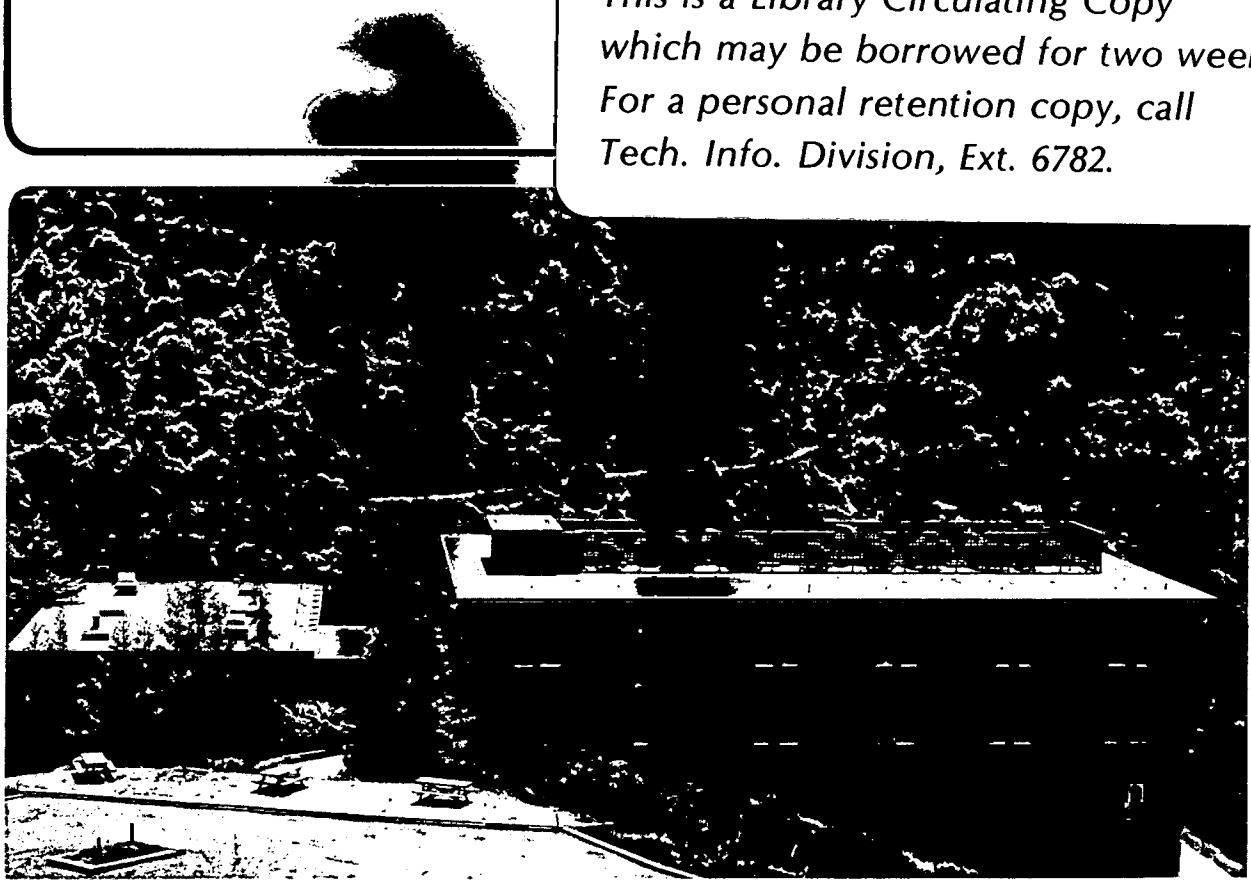

LBL-15435 c.2

DISCLAIMER

This document was prepared as an account of work sponsored by the United States Government. While this document is believed to contain correct information, neither the United States Government nor any agency thereof, nor the Regents of the University of California, nor any of their employees, makes any warranty, express or implied, or assumes any legal responsibility for the accuracy, completeness, or usefulness of any information, apparatus, product, or process disclosed, or represents that its use would not infringe privately owned rights. Reference herein to any specific commercial product, process, or service by its trade name, trademark, manufacturer, or otherwise, does not necessarily constitute or imply its endorsement, recommendation, or favoring by the United States Government or any agency thereof, or the Regents of the University of California. The views and opinions of authors expressed herein do not necessarily state or reflect those of the United States Government or any agency thereof or the Regents of the University of California.

LBL-14535

MICROSTRUCTURES, TRANSFORMATIONS AND PROPERTIES OF OXIDATION-RESISTANT, IRON-BASE, ALUMINUM-MODIFIED ALLOYS

Gustavo Luis Tamayo
(M.S. Thesis)

Materials and Molecular Research Division
Lawrence Berkeley Laboratory
University of California
Berkeley, California 94720

December 1982

This work was supported by the Division of Materials Sciences, Office of Basic Energy Sciences, U.S. Department of Energy under Contract Number DE-AC03-76SF00098.

MICROSTRUCTURES, TRANSFORMATIONS AND PROPERTIES OF OXIDATION-RESISTANT, IRON-BASE, ALUMINUM-MODIFIED ALLOYS

Master of Science Gustavo Luis Tamayo Materials Science

Gareth Thomas
Chairman of Committee

ABSTRACT

The effect of different cooling rates on the microstructure and properties of an Fe-8Al-6Mo-0.25Nb-0.8Zr-0.1Ce-0.1C alloy, initially heat treated at 900°C for one hour, were investigated. Electron diffraction and microscopy revealed that air cooled specimens contain a uniform distribution of second phase particles of approximately 3000Å in diameter consisting principally of Iron, Molybdenum and Niobium. Evidence of DO_3 ordered particles was also found at this cooling rate. Oil-quenched and water-quenched specimens presented a more distorted matrix with a smaller grain size but the presence of second phase particles was not evident.

Mechanical strength and hardness were higher and ductility lower for the slowly cooled specimens. However, oxidation resistance at 1000°C in air showed only slight variation with cooling rate, and compared favorably with two austenitic stainless steels subjected to the same treatment.

It is concluded that the substitution of Aluminum for Chromium and Nickel in Iron-base alloys can be made with little or no loss of favorable microstructures and properties characteristic of stainless steels.

TABLE OF CONTENTS

1. INTRODUCTION. 1

2. EXPERIMENTAL PROCEDURES 4

2.1 Materials Preparation and Heat Treatment 4

2.2 Mechanical Testing 4

2.2.1 Room Temperature. 4

2.2.2 High Temperature. 5

2.3 Oxidation Testing. 5

2.4 Microscopy 6

2.4.1 Optical Metallography 6

2.4.2 Transmission Electron Microscopy. 6

2.4.3 Scanning Electron Microscopy. 7

2.4.2 Auger Electron Spectroscopy 7

3. RESULTS 8

3.1 Composition. 8

3.2 Mechanical Properties. 9

3.2.1 Room Temperature. 9

3.2.2 High Temperature. 10

3.3 Fractography 11

3.4 Oxidation Properties 11

3.4.1 Gravimetric Results 11

3.4.2 Oxide Analysis. 12

3.5 Microstructure 15

3.5.1 Optical Metallography 15

3.5.2 TEM-STEM Analysis 15

4. DISCUSSION. 19

4.1 Mechanical Properties and Microstructure 19

4.2 Oxidation Properties and Microstructure. 21

4.3 Suggestions for Future Work. 24

5. CONCLUSIONS 26

ACKNOWLEDGEMENTS. 27

REFERENCES. 28

TABLES. 31

FIGURE CAPTIONS 33

FIGURES 35

1. INTRODUCTION

In recent years increased attention has been paid to the subject of substitution of strategic materials used in alloy fabrication.[1-3] Strategic materials are those which are unavailable internally to a manufacturing country and which must consequently be obtained by import from foreign countries. Substitution is therefore employed not because of reduced cost, but because of reduced dependence upon external supply of an essential alloying element. These elements are considered critical in many countries around the world because of the high net import-reliance-to-apparent-consumption ratio, since the highest percentages of the world mineral reserves are located in very few countries.[4,5] However, historically the issue of critical materials has been addressed only after shortages have affected manufacturing capabilities. Chromium and nickel, two of the elements most frequently used in high temperature technology and the stainless steel industry, are among these critical materials. Even though these materials are, at present, readily available and relatively economical, alloy research and development programs have been put on alert for "substitution preparedness."[6]

Several investigations have been carried out on iron-aluminum alloys since around 1930,[7-9] when it was discovered that the addition of Aluminum to ferrous alloys greatly improves their oxidation resistance. However, aluminum additions in excess of about 8% were found to make the alloy too brittle to be of commercial value. During

the 1950's, more experiments[10-16] were performed on these alloys in an attempt to establish their mechanical and oxidation properties. More recently, after the concern about critical materials arose, some investigators have been working on the improvement of the high temperature properties of iron-aluminum alloys, but very few have been successful.[17-23] In a program specifically aimed at low cost, high strength, high temperature oxidation-resistant iron-aluminum alloys, Nachman and Duffy[24] achieved notable success. Their program was based upon the addition of refractory elements such as molybdenum, tantalum, niobium and cerium, for solid solution strengthening, along with zirconium and carbon for second phase ZrC strengthening, in order to increase the stress-rupture life of Fe-Al alloys at 815°C (1500°F). It was found that the higher aluminum alloys (10-15 wt% Al) exhibited better oxidation resistance in air, at temperatures up to 980°C (1800°F), than any conventional high temperature alloy. However, these alloys also demonstrated very poor ductility, with elongation values rarely exceeding 5%. Ductility seemed to improve with lower Aluminum content, and an "optimum" was established at 8 wt% Al. The full compositional analysis of this alloy, designated U8, was given as: Fe-8 Al-6 Mo-0.8 Zr-0.25 Nb-0.1 Ce-0.1 C.

This alloy was hot rolled at 1100°C, warm rolled at 700°C, heat treated to 950°C and then furnace cooled to room temperature. Cyclic oxidation properties at 815°C and 980°C, stress-rupture properties at 815°C and 4000 psi, and room temperature properties were measured together with some standard stainless steels for comparison. Its

cyclic oxidation behavior was equivalent to 321 stainless steel at the temperatures studied. Its stress-rupture life of 150 hours was intermediate between the martensitic-ferritic and the austenitic stainless steels, and its room temperature ductility of 16% elongation was acceptable. Unfortunately, however, no microstructural analysis was done on this alloy to identify the reason for its behavior.

The aim of this research is to establish the correlation between microstructure and properties of the above mentioned alloy in an attempt to understand and further improve its high-temperature behavior. For such purpose, three different quenching treatments were applied after heat treatment to induce microstructural variations. Oxidation tests were also performed under isothermic conditions, since there was a lack of information on the behavior of alloy U8 in this situation. These properties were then compared with two stainless steels tested under the same conditions: a type 304 stainless steel, which represents the largest single use for chromium in the U.S.A., and a type 310 heat-resistant stainless steel. Stress-rupture tests were attempted at a slightly higher temperature of 1000°C, and room temperature properties were again measured. These properties were then correlated with details of internal microstructure and external oxide scale using techniques of Optical Microscopy, Scanning Electron Microscopy (SEM), Transmission Electron Microscopy (TEM), Scanning Transmission Electron Microscopy (STEM), Auger Electron Spectroscopy (AES) and Energy Dispersive X-ray Spectroscopy (EDXS).

2. EXPERIMENTAL PROCEDURES

2.1 Materials Preparation and Heat Treatment

The alloy used in this work has the following nominal composition: Fe-8 Al-6 Mo-0.8 Zr-0.25 Nb-0.1 Ce-0.1 C. Two 250 gr. cast buttons were produced by standard vacuum melting practice at LBL facilities. Each of the buttons underwent the thermo-mechanical treatment schematically illustrated in Fig. 1. They were homogenized for 24 hours at 1200°C and then hot-rolled at 1100°C to about 1.5 mm in thickness. From this flat sheet, rectangular specimens were cut off in the rolling direction with dimensions slightly larger than those of the subsize specimens specified in the ASTM standard methods of tension testing (E8) and creep-rupture tension testing (E150-64). These blank specimens were placed into stainless steel bags, separated into 3 groups and heat treated to 900°C for one hour. Each group then received a different cooling treatment: air cooling, oil quench and iced brine, respectively. Following this, they were machined to standard ASTM dimensions.

2.2 Mechanical Testing

2.2.1 Room Temperature. Tensile flat specimens of the dimensions shown in Fig. 2 were used for tension tests with an MTS testing machine using a 1000 kg load at a cross head speed of 0.8 in/min and a strain rate of 0.05 in/in. Rockwell hardness tests were conducted on the broken tensile samples with a 1/16"-diameter steel ball and a 100 kg-major load (B scale).

2.2.2 High Temperature. Stress-rupture tests were performed at 1000°C on specimens similar to the tensile test specimens. They were heated to uniform temperature and then loaded to a equivalent stress of 4000 psi to determine rupture life and elongation.

2.3 Oxidation Testing

The oxidation rate measurements were carried out in air at 1000°C in a resistance-wound horizontal-tube furnace for up to 30 hours. Specimens of about 10x6x1 mm were abrasively cut from the end sides of the broken tensile samples and then ground down on 600 grit SiC paper. They were degreased with acetone, measured to the nearest tenth of a millimeter and weighted with an accuracy of 0.1 mg. The specimens were suspended inside individual alumina crucibles by a fine platinum wire which was inserted through a hole drilled in the specimens and wound around the crucibles. Wire and crucibles were also weighed with the same accuracy. The crucibles plus specimens were covered with alumina lids and placed inside an alumina boat for positioning within the uniform temperature zone of the furnace ($\Delta T \sim 4°C$). The loading time for positioning and preheating was about 25 min (~0.5 cm/min); the unloading time for retrieving and cooling was about 15 min (~1 cm/min). After cooling to room temperature, the specimens were weighed together and separately from the crucibles to establish weight gain differences. Systematic and random error were considered by calculating a standard deviation (σ) and placing the results within a range of 2σ.

2.4 Microscopy

All the specimens for microscopy were obtained from the end sides of the broken tensile samples. Gripping marks were removed by grinding on an horizontal magnetic grinder if necessary.

2.4.1 Optical Metallography. Specimens were abrasively cut under flood cooling to be examined over the flat faces parallel to the rolling direction and across the cross-sectional area. They were mounted in bakelite or kold-mount, rough-ground on a flood-cooled 240 grit belt and then hand ground on wet SiC paper to 600 grit. The fine grinding was done on a polishing wheel with a canvas cloth and 6 μ diamond paste, and then 1 and 0.3 μ alumina were used on a felt microcloth. Etching was done with a solution of 7.5% HNO_3, 2.5% HF in distilled water containing a few grains of potassium-ferrocyanide.

2.4.2 Transmission Electron Microscopy. Thin foils of about 5 mils were obtained by chemical thinning, at room temperature, in a solution of 4% HF in H_2O_2 from the 1 mm (~40 mils) thick tensile specimens. Then, 3 mm discs were punched out from the foils and hand ground on 600 grit SiC paper to about 2-3 mils to remove any oxide layer. TEM discs were prepared by jet electropolishing. The electrolyte consisted of 1 part nitric acid and 2 parts methyl alcohol. Polishing conditions were: 5-10 V, 15-20 mA, -30 to -40°C and low jet velocity to avoid preferential polishing of the periphery of the discs. The specimens were stored in 200 proof ethyl alcohol and subsequently examined in a Siemens 1A and a Phillips EM301 electron microscopes, both operating at 100 KV. Subsequently, STEM and EDXS analysis were

performed using a Phillips EM400 electron microscope with X-ray microanalysis capability.

2.4.3 Scanning Electron Microscopy. After-test oxidation specimens were mounted in a cold-setting resin. Bakelite-fiber pieces were inserted around the specimens to protect the oxidation product for image and semi-quantitative chemical analysis using an AMR-1000 scanning electron microscope operating at 20 kv. A KEVEX energy dispersive analysis unit, attached to the microscope, was used to determine the relative composition of the particles observed in the microstructures. X-ray microanalysis was also performed on the alloy at stage A in Fig. 1, through the cross-section of hot-rolled specimens, to establish differences in composition.

The fracture surface of the broken tensile samples were also examined with this microscope to determine the crystallographic mode of the fracture.

2.4.4 Auger Electron Spectroscopy. A scanning Auger microscope was used to analyze the different oxide layers on the oxidation specimens. The specimens were mounted in kold-mount, polished down with 0.3 μ alumina along the cross-section and then removed from their mounting with a strong solvent. Chemical mapping as well as probe-point analysis were carried out to determine the nature of the scales and features observed in the microstructure.

3. RESULTS

In order to simplify presentation of the results obtained, the specimens studied will be referred to as AC, OQ and IB for the three different cooling treatments applied to the alloy, i.e., air cooling, oil quench and iced brine quench, respectively. The baseline alloy which underwent a furnace cooling treatment will continue to be referred to as U8. Chemical compositions will always be specified in weight percent, unless otherwise indicated.

3.1 Composition

The chemical composition of the alloy after homogenization and hot rolling (point A in Figure 1), was obtained by emission spectrography. The results are shown in Table I, wherein they are compared to the nominal composition of the alloy U8. Although both alloys are fairly similar in composition, there are some notable differences. For example, the Ce content in the new alloy is considerably lower than in alloy U8. This element is added to the alloy for high temperature oxidation resistance and its deficiency may negatively affect the oxidation behavior of this alloy. Another point reported earlier[24] was the improved room temperature ductility of alloys with Ce additions.

Although the Mo content is not so different in the new alloy from that of alloy U8, Nachman and Duffy[24] emphasize the need for a 6% Mo content, particularly for 980°C service. Also, with respect to the Al content, the positive difference in the new alloy may represent a gain in oxidation properties over U8 but it also means that there is a

higher quantity of Al available for the formation of second phase Fe_3Al, DO_3 type ordered particles, observed in previous work,[25-27] which can reduce the room temperature ductility of the alloy.

3.2 Mechanical Properties

3.2.1 Room Temperature. The mechanical properties of the alloy at room temperature are summarized in Table II. It was observed that the strength and hardness of the alloy increased, and the ductility decreased, upon reducing the cooling rate. Table II also shows the mechanical properties of alloy U8 reported by Nachman and Duffy.[24] As mentioned before this alloy received an even slower cooling treatment, i.e., furnace cooling, and nonetheless its yield strength is lower and its ductility higher than alloy AC. This relationship between strength, ductility and cooling rate is more clearly visualized in Fig. 3. Here, the cooling rates were estimated from a previous study[28] where they were measured by a thermocouple in the center of the specimen and recorded by a strip chart recorder. The error bars on the strength and ductility values represent a 2σ deviation (σ = standard deviation) based upon three tests performed for each case. There is also a clear relationship between the ratio YS/UTS and ductility, i.e., the ductility decreases as the ratio YS/UTS approaches unity.

Table II also shows two other values of mechanical properties reported earlier,[24] alloys U9 and U12. Both alloys underwent the same heat treatment as alloy U8, but had very small differences in composition. Alloy U9 has the composition of alloy U8 (Table I) plus

0.5% Si. This variation resulted in a considerable increase in strength and hardness, with an equally important decrease in ductility. Alloy U12 did not contain Ce and its ductility was even lower. Thus, even small changes in composition of the quaternary elements of the alloy can be very effective in varying its properties as mentioned in Section 3.1.

3.2.2 High Temperature. The mechanical properties of the alloy at 1000°C were obtained from stress-rupture tests carried out with an applied stress of 4000 psi. It was found that this stress was too severe at the temperature indicated since the rupture life values were extremely short. This fact is corroborated by Parker[29] who listed maximum values of initial stress during stress-rupture tests at 1000°C which were 3000 psi for austenitic stainless steels and 700 psi for ferritic stainless steels. Jahncke and Frank[30] point out maximum useful temperatures for stainless steels of 56% and 63% of the melting point for ferritic and austenitic steels, respectively. The present study was conducted at about 67% TM, which is a relatively high value. Nevertheless, the rupture-life-to-elongation ratio of the alloy AC is higher than the OQ and IB alloys. Smith[31] suggests that this ratio is an empirical indicator of an average creep rate. Thus, alloy AC seems to possess a better resistance to elongation at high temperature.

The results of stress-rupture tests at 815°C of the alloys U8, U9 and U12 are also given in Table II. The impressive values of alloy U8 at about 54% TM are intermediate between the martensitic/ferritic and the austenitic stainless steels[29] and make this alloy very attractive

for high temperature use. The values of alloys U9 and U12 in comparison to U8 again reveal the importance of the quaternary elements on the behavior of the alloy.

3.3 Fractography

The fracture surface of the broken tensile samples from the room temperature tests were observed in the Scanning Electron Microscope (SEM) to determine the crystallographic mode of the fracture. In general, as seen in Fig. 4, the surfaces of specimens subjected to all three cooling rates, i.e., AC, OQ and IB specimens, have the characteristic appearance of brittle fracture with a granular resemblance and the "river patterns" of branching cracks related to transgranular cleavage surfaces. However, the AC fractures seem to exhibit a higher quantity of microcracks than OQ and IB fractures.

3.4 Oxidation Properties

3.4.1 Gravimetric Results. The results of the gain in weight as a function of $(\text{time})^{1/2}$ in air at one atmosphere and 1000°C are plotted in Fig. 5 for the new alloy, as well as two austenitic chromium-nickel stainless steels, a type 304L and a type 310, oxidized under identical conditions. The oxidation behavior of the Fe-Al alloy was intermediate between the stainless steels, as represented by the banded region in the figure. The limits of this region represent a range of 2σ as calculated from the two weight measurements performed on each specimen. The variation in oxidation resistance among the three differently-cooled alloys was very small. However, at every point in time there always was a sequence followed in weight gained, i.e.,

AC-OQ-IB in increasing order. Thus, three tentative lines are drawn within the banded region of the figure, which suggest that the oxidation resistance is generally better for the slowly-cooled alloys. The type 304L steel that was tested together with the Fe-Al alloys showed poorer oxidation behavior with a large amount of spalled oxide and a higher oxidation rate. Spallation was not observed on the type 310 stainless steel.

3.4.2 Oxide Analysis. Metallographic examination of the cross-section of the oxidized specimens confirmed an increase in scale thickness with time. Furthermore, specimens of the new alloy showed a variation in oxide type on the opposite faces of the sheet specimens. An example of this behavior is shown in Fig. 6. The top SEM micrograph shows a thin oxide layer on an AC specimen oxidized for 30 hours at 1000°C. Small arrows indicate the presence of oxide intrusions extending into the alloy substrate, which is indicative of a good scale-alloy adherence.[32] Also, different types of inclusions are visible in this side of the cross section, together with some porous areas from which some inclusions may have been etched away. The bottom micrograph of Fig. 6 shows the other side of the cross-sectional area, with an oxide between three and four times thicker and with a two-layered appearance. It is also noted that on this side of the specimen there were no visible inclusions.

Figure 7 shows an optical micrograph of this section of the alloy, after homogenization and hot rolling at stage A in Fig. 1, where an EDXS electron microprobe analysis was performed on the points signaled

by the circles. The corresponding quantitative results are shown beneath the micrograph. It is clear that the aluminum content decreases and the molybdenum content increases from top to bottom of the micrograph. It is important to note that cerium was detected on the top side, since additions of this element to high temperature alloys have been shown to increase their oxidation resistance.[33] Moreover, the present alloy is very sensitive to variations of cerium and molybdenum content, as pointed out earlier in Sections 3.1 and 3.2.

The difference in inclusion content between top and bottom of the specimen is also clear in Fig. 7. Figure 8 shows higher magnification photographs of the top side of Fig. 7, where the inclusions have similar morphology to the ones observed in the thin oxide side of the oxidized specimens. This suggests that the inclusions did not dissolve even after the heat and oxidation treatments were applied to the alloys. The inclusions ranged in sizes of about 0.1 microns to about 7 microns, with some of the small ones decorating the grain boundaries.

An EDXS analysis was performed on some of these inclusions and is shown in Fig. 9. The inclusions obviously contained high quantities of refractory elements such as Zr and Ce as well as Fe. Particles with an equiaxed shape such as particle 1 possessed high percentage of Ce, while particles with a more elongated shape were Zr-rich. In order to more precisely reveal the nature of these inclusions an Auger electron microscope was used, since the above X-ray emission techniques are limited to detect those elements of atomic number (Z) greater than about 11. Elements such as C and O can be measured using the AES

technique and in this way the inclusions proved to be chiefly oxides and carbides of the above-mentioned elements, which probably formed during the melting process. Using the same technique, the distribution of the principal elements of the alloy was mapped in each side of the cross-section, as shown in Figs. 10(a) and 10(b) for an AC alloy oxidized for 30 hours at 1000°C. Figure 10(a) clearly shows a fine outer oxide layer rich in Fe with an inner, thicker Al-rich oxide layer protruding into the alloy. Note also that there are some Al-rich areas extending to the center of the cross-section. Figure 10(b) shows an inverse distribution of the oxide layers, i.e., a thick outer layer rich in Fe and an inner, thinner layer rich in Al with no clear protusions into the alloy.

A point analysis of the distribution of the elements in both oxides was performed with the Auger electron microscope by doing microprobe analysis at different distances from the oxide-atmosphere interface. These are shown by the encircled white dots in Fig. 11(a), with the qualitative results given in Fig. 11(b). It is obvious that Al is not clearly detected in the thick scale until point 3, diminishing in percentage into the matrix where spectra 4 and 5 were similar. A considerable amount of C and some Mo content are present, along with high quantities of Fe, in the outer layers. By comparison, the thin oxide layer is seen to consist mainly of Al and O. Point 2 was placed over one of the oxide pegs, which showed a higher quantity of Al and some C content. Further into the alloy, at points 3 and 4, the Fe and Mo content increased while the Al content decreased.

3.5 Microstructure

3.5.1 Optical Metallography. The microstructures of the three differently cooled alloys, at low magnification, are presented in Fig. 12. The grain size in sample IB is smaller than in the OQ and AC samples, as expected from its more rapid cooling treatment. The small particles seen in the three samples were observed at higher magnifications where they resembled the inclusions mentioned in Section 3.4. Some remnant pieces of alloy U8, donated by J. F. Nachman from the original tensile bars used in his research,[24] were also examined for comparison of the microstructures. Figure 12 shows the microstructure of U8 where the grain size is comparable to the IB alloy. Although no inclusions were noticed here, some second phase particles were observed in the grains, and decorating the grain boundaries.

3.5.2 TEM-STEM Analysis.

3.5.2.1 IB samples. The microstructure of this specimen is given in Fig. 13 where an area of small grains with a high density of dislocations and slip bands is observed. Figure 14 is a higher magnification image illustrating the origin[34] of the slip bands at the grain boundary region.

3.5.2.2 OQ samples. The microstructures of these specimens also showed high density of dislocations but with an increased tendency to form dislocation substructures and small boundaries, as shown in Fig. 15. Figure 15(a) is a BF micrograph showing small angle boundary pinning at a second phase particle. Figure 15(b) represents a weak beam dark field (WBDF) of the same area where the geometry of the dislocations becomes clearer. Higher magnification images of the boxed

region from Fig. 15(a) are also given in Fig. 16 to more clearly show the detailed dislocation configurations. An EDXS analysis of the particle in Fig. 15(a) is given in Fig. 15(c), where the analysis was performed on the particle and on the adjacent matrix for comparison, using an electron probe of 400 Å in diameter. The particle did not contain appreciable quantities of Fe, Al or Mo as compared to the matrix, but contained mainly Zr and some Nb. These quantitative results matched those shown in Fig. 9, and suggests that this particle is a Zr-rich inclusion.

3.5.2.3 AC samples. The microstructure of these samples exhibited a matrix which was less distorted than the two previous specimens but which contained some homogeneously distributed particles. These particles ranged in size from 0.5 microns to about 3 microns with a few of them present at the grain boundaries, as shown in Fig. 17(a). In order to determine the nature of these particles and their orientation relationship with the matrix, electron diffraction and EDXS analyses were performed in a transmission electron microscope. Figure 18(a) shows a selected area diffraction (SAD) pattern taken from a typical area such as Fig. 17(a). In this micrograph there are two superimposed patterns present: the matrix pattern identified as $[\bar{1}13]_F$ which is from the bcc ferrite phase and the particle pattern identified as $[\bar{7}41]_p$, which is from the diamond cubic M_6C phase. A center dark field (CDF) image of the particle shown in Fig. 18(b) was obtained using the reflection indicated in Fig. 18(a). To corroborate the identification of these carbides in

the matrix of the AC samples, several microdiffraction patterns were obtained from several particles in Fig. 17(a). Two of these are shown in Figs. 17(b) and 17(c). Again, the patterns were found to be associated with M_6C carbides in $[477]_p$ and a $[001]_p$ orientations, respectively. The composition of these particles was determined by X-ray microanalysis, with a probe diameter of 400 Å as shown in Fig. 19. The corresponding spectra of each particle are shown at the bottom of the micrographs, where it is obvious that the carbides possess a high content of Fe with some Al. It is also clear that high quantities of the carbide-formers Mo and Nb are present, while the Cu and Cr signals are present in the background. The quantitative analysis of the above-mentioned particles shows best agreement with the stoichiometry of M_6C carbides. Also, at the C and Mo levels contained in the alloy (0.1% and 6%, respectively), the formation of M_6C carbides agrees with the ternary equilibrium Fe-Mo-C phase diagram.[35]

Some evidence of DO_3 ordering was found in the AC samples, as shown in Fig. 20. Here, the [001] SAD pattern of the ferrite phase showed weak and diffuse 100 type superlattice reflections from which the CDF image of Fig. 20(c) was obtained.

3.5.2.4 U8 samples. The microstructure of this alloy was similar overall to that of the AC samples described above. Figure 21(a) shows a typical area where the same type of particles are seen. These particles were also homogeneously distributed throughout the matrix and grain boundaries but they were slightly larger, ranging from 2 microns to 7 microns in size. Microdiffraction and

microanalysis again revealed that these paticles were M_6C carbides, rich in Fe, Al, and Mo and Nb, as shown in Figs. 21(b) and 22.

The presence of the DO_3 type ordered particles in these alloys was much more definite, as shown in the [001] SAD pattern of Fig. 23, where the superlattice reflections of the DO_3 structure are very clearly resolved (c.f. Fig. 20). The CDF image of these particles in this case was consequently also better resolved, as seen in Fig. 23(c) where the particles appeared to be aligned parallel to the $\langle\bar{1}10\rangle$ projection, in accordance with previous work.[25-27]

4. DISCUSSION

4.1 Mechanical Properties and Microstructure

The mechanical properties of the alloys studied, summarized in Fig. 3, indicate an obvious increase in strength as the period of time to cool down to room temperature from 900°C is increased. The strength undergoes a peak for the air cooling treatment but then it decreases when the alloy is subjected to prolonged furnace cooling (alloy U8). These facts suggest that strengthening may be produced by age hardening through precipitation of second-phase particles, in addition to any solid solution strengthening which may result from the extensive alloy additions. From the microstructural results it is noted that M_6C carbides were observed in the AC and U8 samples but not in the OQ or IB samples. These carbides most probably precipitated upon slow cooling from 900°C. Carbide precipitation during slow cooling has also been observed in controlled rolled low carbon steels containing Nb[36]. The larger size of these carbides after furnace cooling plus the decrease in strength suggest that an overaging process has occurred with respect to the air cooling treatment.

It is clear from an analysis of the larger carbide particles in these samples that they are simply too coarse (~3 microns) to contribute significantly to strengthening. Furthermore, their interfacial structure is characteristic of fully incoherent boundaries, which for this size of particle, are also poor strengtheners. However, there is evidence of a large amount of smaller carbide particles

(see Fig. 17) in the stronger samples which were not evident in alloy U8. These small particles are most likely the major source of precipitation hardening.

The strengthening of the OQ and IB samples may be produced by dislocation mechanisms involving subgrain boundaries as mentioned previously in Section 3.5.2. Furthermore, the suggestion of pinning (arrowed in Fig. 16(b)) might be used to explain the higher yield strength of the OQ samples over the IB samples. Here again it is suspected that the slower oil quench may have induced a fine carbide precipitation which was suppressed by the more rapid iced brine quench.

There may also be a secondary hardening mechanism acting in these alloys, induced by the ordering process occurring in the slowly cooled samples. Some Fe-Al alloys have been observed to exhibit very small ordered particles, with the DO_3-type structure after quenching and aging. These particles have characteristic strain-contrast images and electron diffraction effects,[25-27] and most importantly show localized-strain fields along <110>, or <100> depending on the foil normal and on the operating reflection. As reported in Section 3.5.2, the ordered superlattice reflections were better resolved in the furnace cooled U8 sample than in the AC sample and were not found in the OQ and IB samples. This is most likely the result of an increased volume fraction of the ordered phase with slower cooling rate.

It is clear that this hardening mechanism is less effective than the precipitation of carbides since the yield stress actually decreased for the U8 sample. It is also obvious that the grain size influence on

strengthening is less important than the carbide precipitation reaction, as illustrated in Fig. 12 where the largest grain size is found in the AC sample, which nonetheless showed the highest resistance to yield. This fact is further corroborated by the smaller grain size and the lower strength exhibited by the U8 sample.

It is also apparent, that the mechanical properties of the new alloy at 1000°C were very poor and there was no clear difference in behavior among the three different cooling treatments. However, the AC sample exhibited a better creep behavior by its higher rupture life/elongation ratio. This may be explained by the fact that the matrix slip was retarded by the presence of the M_6C carbides while grain boundary slip was inhibited by larger grain size of the AC samples.

In addition, the relatively higher quantity of microcracks found in the AC sample (Fig. 4) represents a higher quantity of particle-forming microcracks. The M_6C carbides are again thought to play a significant role here, since they were present at grain boundaries as well as in the matrix grains in the same distribution as that of the observed microcracks.

4.2 Oxidation Properties and Microstructure

The three samples of the Fe-Al alloys tested exhibited at any time in these experiments two kinds of oxide scales. As such the results represent a variation in the oxidation properties which are possible for these alloys. This unconventional oxidation behavior is obviously due to a composition gradient from one side of each sample to the

other across its cross-sectional area, as seen in Figs. 7 and 11. These analyses showed that in the thick oxide side there was a high content of Mo present. As mentioned earlier in Section 3.1, the properties of these alloys have been shown[24] to be very sensitive to the presence of this element. Specifically, oxidation resistance is drastically decreased when the Mo content increases beyond 6%. Also, the Al content necessary for the formation of an Al-rich protective oxide, obtained from these analyses in the thick oxide side was considerably lower than in the thin oxide side. Some authors[37,38] point out that at 1000°C the initial oxide layer formed on the surface of Fe-Al alloys appears to be a solid solution of Al_2O_3 and Fe_2O_3 which is rich in any of these two phases depending on the quantity of Al available in the substrate. These facts tend to indicate that the thick oxide scale may have the composition of an Fe_2O_3-rich oxide and that the thin oxide scale may have the composition of an Al_2O_3-rich oxide. The chemical maps of Fig. 10 obtained by the AES technique further confirm this theory. The thick oxide scale not only appeared to be very thick but also gave evidence of poor adherence to the substrate. Some areas of the scale in fact exhibited a gap in continuity and no peg-like features were observed there. On the other hand, the thin oxide scale was both continuous and marked with peg-like oxide protrusions indicative of good adherence to the substrate.[32] The other important features observed in this side were the Zr-rich and Ce-rich inclusions present in the grains and along the grain boundaries. This is a significant fact since it has been reported[33] that

the dominant oxygen transport mechanism in the oxidation of Al_2O_3-forming alloys is via grain boundary short circuit paths. Thus, these inclusions may assist in reducing the scale growth rate.

The gravimetric results from the isothermic oxidation tests plotted in Fig. 5 showed only slight variation with cooling rate. The form of these curves suggests a parabolic type of oxidation behavior which is usually associated with a diffusion-controlled oxidation mechanism.[39] The rate of oxidation is controlled by either cation or anion diffusion across the barrier film. If the process is diffusion-controlled the weight gained (wg) can be approximated by:

$$wg = Kd\sqrt{4Dt}$$

where K = a dimensionless function of the driving force

d = density

D = diffusion coefficient

t = time.

Therefore, in a plot of w.g. vs. $t^{1/2}$, the slope gives the value $Kd\sqrt{4D}$, which is an indicator of the oxidation kinetics. From Fig. 5 it is obvious that the Fe-Al alloys underwent an intermediate oxidation behavior between the austenitic stainless steels. Also, it would appear that the AC samples exhibited better oxidation resistance than the OQ or IB samples. The M_6C carbides present in the matrix and grain boundaries of the AC samples may be adding to the effect of the Zr and Ce-rich inclusions mentioned above. These carbides also showed a high content of Mo by which the respective decrease of this element in the surrounding ferrite matrix could be a positive influence on its

oxidation resistance. Moreover, if the Al-rich oxide growth is determined by the oxygen diffusing into the alloy via grain boundary short circuit paths, the larger grain size and consequently the reduced grain boundary area of the AC samples may be directly responsible for their apparently better oxidation resistance.

4.3 Suggestions for Future Work

To further improve and understand the behavior of these Fe-Al alloys the following suggestions have developed from this analysis:

a) An investigation should be undertaken of alloys with higher Ce content, since these hold the promise of better oxidation properties.

b) Aluminum contents up to 9% might be studied for a possible increase in oxidation resistance with no attendant loss in ductility.

c) An adjustment of the Nb to Mo ratio should be investigated for its effect on oxidation resistance. A balance of these two elements may improve oxidation resistance by decreasing the Mo content, without sacrificing strength through formation of niobium carbides.

d) A slight increase in the inclusion-forming element Zr might also be tried for enhanced oxidation resistance.

e) An aging treatment after iced brine quenching would be worth comparing to simple air cooling, since this would help to establish differences in both the precipitation and ordering processes.

f) Elevated-temperature stress-rupture tests should be performed at slightly lower temperatures in differently cooled samples to determine the relationship between cooling rate and high temperature strength.

5. CONCLUSIONS

1. The Fe-Al alloys studied in this work exhibited microstructures, mechanical properties and oxidation properties that compare favorably with 300-series stainless steels.
2. Slight variations in composition of alloying elements such as Mo have a considerable effect on the oxidation behavior of these alloys.
3. A large grain size and the presence of refractory Zr and Ce inclusions seem to provide these alloys with enhanced oxidation resistance.
4. Compositional analysis on the oxidized alloys has established that Al diffuses to the surface and forms an Al-rich oxide.
5. The most effective strengthening mechanism acting on these alloys appears to be the precipitation of M_6C carbides upon slow cooling from 900°C. A small grain size is less important overall than precipitation hardening on the resistance to yield.
6. The presence of small second phase DO_3-ordered particles was confirmed in the slowly cooled alloys.
7. The crystallographic mode of the fracture of these alloys at room temperature is of the cleavage type.
8. An air cooling treatment from 900°C seems to yield the best properties of these alloys. However, if one is willing to sacrifice some strength, better ductility can be achieved by a faster cooling treatment.

ACKNOWLEDGEMENTS

I gratefully acknowledge the constant support and encouragement of my wife, Nahir, throughout the development of this research. This work is especially dedicated to her and to my parents, Juan and Nena.

The author wishes to express his sincere gratitude to Dr. Ronald Gronsky for his valuable guidance, encouragement, patience and friendship. Special thanks are due to all his colleagues and friends, in particular to Mehmet Sarikaya, Kannan Krishnan, Hillary Akuezue, Gianni Fior and Eduardo Kamenetzky for their useful help, stimulating discussions and sporting friendship.

The able assistance of the support staff of the Materials and Molecular Research Division of the Lawrence Berkeley Laboratory is also gratefully appreciated. In particular to John Holthuis, John Jacobsen, Weyland Wong, Ken Gaugler and Erlene Fong.

The author also wishes to thank Professors Gareth Thomas and Israel Cornet for their suggestions and appraisal of this manuscript.

Financial support during the course of this work was provided by the Fundacion Gran Mariscal de Ayacucho, Venezuela. The research facilities at the Lawrence Berkeley Laboratory are funded by the Division of Materials Sciences, Office of Basic Energy Sciences, U.S. Department of Energy, under Contract No. DE-AC03-76SF00098.

REFERENCES

1. A. G. Gray, Metal Progress, Nov. 1981, p. 25.
2. A. G. Gray, Metal Progress, Dec. 1981, p. 15.
3. A. G. Gray, Metal Progress, Jan. 1982, p. 11.
4. Mineral Facts and Problems, U.S. Bureau of Mines, Bulletin No. 650 (1970).
5. Staff report, Metals Week, May 1980, p. 2.
6. A. G. Gray, Metal Progress, Dec. 1981, p. 18.
7. A. Hauttmann, Stahl und Eisen 51, 65 (1931).
8. N. A. Ziegler, Trans. AIME 100, 267 (1932).
9. C. Sykes and W. Bampfylde, J. Iron and Steel Inst. 130, 389 (1934).
10. J. F. Nachman and W. J. Buehler, U.S. Naval Ordnance Lab, NAVORD Report No. 2819 (1953).
11. J. F. Nachman and W. J. Buehler, U.S. Naval Ordnance Lab, NAVORD Report No. 3700 (1954).
12. S. Case and K. R. Van Horn, "Aluminum in Iron and Steel," Ed. Wiley, New York (1954).
13. W. Justusson, V. F. Zackay and E. R. Morgan, Trans. ASM 49, 905 (1956).
14. J. F. Nachman and W. J. Buehler, U.S. Naval Ordnance Lab., NAVORD Report No. 4237 (1956).
15. F. Kayser, Wright Air Development Center, Technical Report No. 57-298 (1957).

16. J. L. Ham and R. E. Cairns, Jr., Product Engineering 29, 50 (1958).

17. D. J. Schmatz, Trans. ASM 52, 898 (1960).

18. L. I. Shvedov and G. P. Goretskii, Vestsi Akad. Navuk Belaruskai SSR (Fiz-Tekhn.) 1, 43 (1972).

19. E. V. Petitbon and J. F. Wallace, AFS Cast Metals Research J. 9, 127 (1973).

20. L. I. Shvedov and G. P. Goretskii, Struktura I Svoisstva Met. I Spalov J, 199 (1974).

21. J. F. Nachman and E. R. Duffy, Corrosion Journal 30, 357 (1974).

22. S. K. Banerji, Metal Progress, Apr. 1978, p. 59.

23. J. R. Stephens, NASA Lewis Research Center, paper presented at the "Public Workshop on Conservation and Substitution Technology for Critical Materials," Vanderbilt University (June 1981).

24. J. F. Nachman and E. R. Duffy, Bureau of Mines OFR 112-76, PB259253 (1976).

25. R. G. Davies, J. Physics Chem. Solids 24, 985 (1963).

26. D. Watanabe, H. Morita, H. Saito, and S. Ogawa, J. Phys. Soc. Japan 25, 293 (1968).

27. H. Warlimont and G. Thomas, Metal Science J. 4, 47 (1970).

28. A. Nakagawa, M.S. thesis, LBL-12843, University of California, Berkeley (Jun. 1981).

29. T. D. Parker, Metals Eng. Quarterly, May 1968.

30. L. P. Jahncke and R. G. Frank, Metal Progress, Nov. 1958, p. 77.

31. G. W. Smith, "Properties of Metals at Elevated Temperatures," 151, McGraw-Hill, New York (1950).

32. D. P. Whittle and J. Stringer, Phil. Trans. Roy. Soc. Lond. A295, 309 (1979).

33. K. N. Strafford and J. M. Harrison, Oxid. Metals 10, 347 (1976).

34. P. J. Worthington and E. Smith, Acta Met. 12, 1277 (1964).

35. "ASM Metals Reference Book," ASM Editorial Staff, ASM Metals Park, Ohio, p. 379 (1981).

36. R. B. Nicholson in "Strengthening Methods in Crystals," p. 582, A. Kelly and R. B. Nicholson, Elsevier Publishing Co., New York (1971).

37. L. M. Atlas and W. K. Sumida, J. Am. Ceram. Soc. 41, 150 (1958).

38. F. Saeguza and L. Lee, Corrosion 22, 168 (1966).

39. J. C. Garcia, N. Rosas and R. J. Rioja, Metal Progress, Aug. 1982, p. 47.

Table I. Alloy composition.

Alloy Designation	Composition, wt%						
	Fe	Al	Mo	Zr	Nb	Ce	C
U8	Bal.	8.00	6.00	0.80	0.25	0.10	0.10
AC, OQ, IB	Bal	8.25	6.22	0.72	0.22	0.075	0.096

Table II. Mechanical properties.

	Room Temperature					High Temperature*		
Alloy Designation	UTS ksi	YS, ksi	YS/UTS	Total Elong. %	Hardness RC	Rupture Life Hours	Elong. %	Rupt. Life/Elong.
AC	92	77	0.84	7.5	18.6	0.05	68	74×10^{-5}
OQ	85	69	0.81	8.6	15.7	0.03	61	49×10^{-5}
IB	83	64	0.77	8.8	11.7	0.05	72	69×10^{-5}
U8	93	70	0.75	15.5	21	150	70	2.14
U9	103	86	0.83	6.0	27	75	35	2.14
U12	89	76	0.85	4.5	24	9.7	120	0.08

*Test temperatures were 1000°C for AC, OQ, IB and 815°C for U8, U9, U12. Applied stress was 4000 psi in all cases.

FIGURE CAPTIONS

Fig. 1. Alloy thermomechanical and heat treatments: schematic.

Fig. 2. Schematic drawing of rectangular tension test specimen.

Fig. 3. Comparison of room-temperature mechanical properties for alloys studied.

Fig. 4. SEM fractographs of tensile specimens.

Fig. 5. Isothermic oxidation at 1000°C plotted as weight gain vs. $time^{1/2}$ for alloys studied.

Fig. 6. SEM micrographs of sample AC oxidized for 30 hours at 1000°C.

Fig. 7. Optical micrograph and EDXS analysis of the cross-sectional area of the alloy after homogenization and hot rolling.

Fig. 8. High magnification SEM micrographs of inclusions present in the homogenized and hot rolled specimens.

Fig. 9. SEM micrograph and corresponding EDXS analysis of the labeled inclusions.

Fig. 10. AES chemical mapping of Fe, Al and O_2 in the cross-section of sample AC oxidized for 30 hours at 1000°C: a) thin oxide side; b) thick oxide side.

Fig. 11. Auger micrographs of oxide scales of sample AC oxidized 30 hours at 1000°C, showing the sites of AES probe-point analysis. a) Top: thin oxide side. Bottom: thick oxide side. b) Corresponding AES spectra.

Fig. 12. Optical micrographs of the alloys studied.

Fig. 13. Low magnification TEM micrograph of sample IB.

Fig. 14. Higher magnification TEM micrographs of sample IB.

Fig. 15. Low magnification TEM micrograph of sample OQ showing the probe site of the EDXS analysis. a) BF. b) WBDF. c) EDXS spectra.

Fig. 16. Higher magnification TEM micrograph of the boxed area in the previous figure. a) BF. b) WBDF.

Fig. 17. a) BF of particles present in the AC alloys. b) and c) Microdiffraction patterns of two of these particles.

Fig. 18. a) SAD pattern of a typical area in the microstructure of the AC alloy showing the orientation relationship between matrix and precipitate. b) CDF image from the reflection indicated in a).

Fig. 19. BF micrographs and correspondent EDXS spectra of two different particles in the AC sample.

Fig. 20. a) BF. b) SAD. c) CDF micrographs of matrix and DO_3 ordered particles in sample AC.

Fig. 21. a) BF of particles present in the U8 alloy.
b) Microdiffraction pattern of one of these particles.
c) Microdiffraction pattern from the matrix.

Fig. 22. BF micrograph and corresponding EDXS spectrum of a particle in the U8 alloy.

Fig. 23. a) BF. b) SAD. c) CDF micrographs of matrix and DO_3 ordered particles in the U8 alloy.

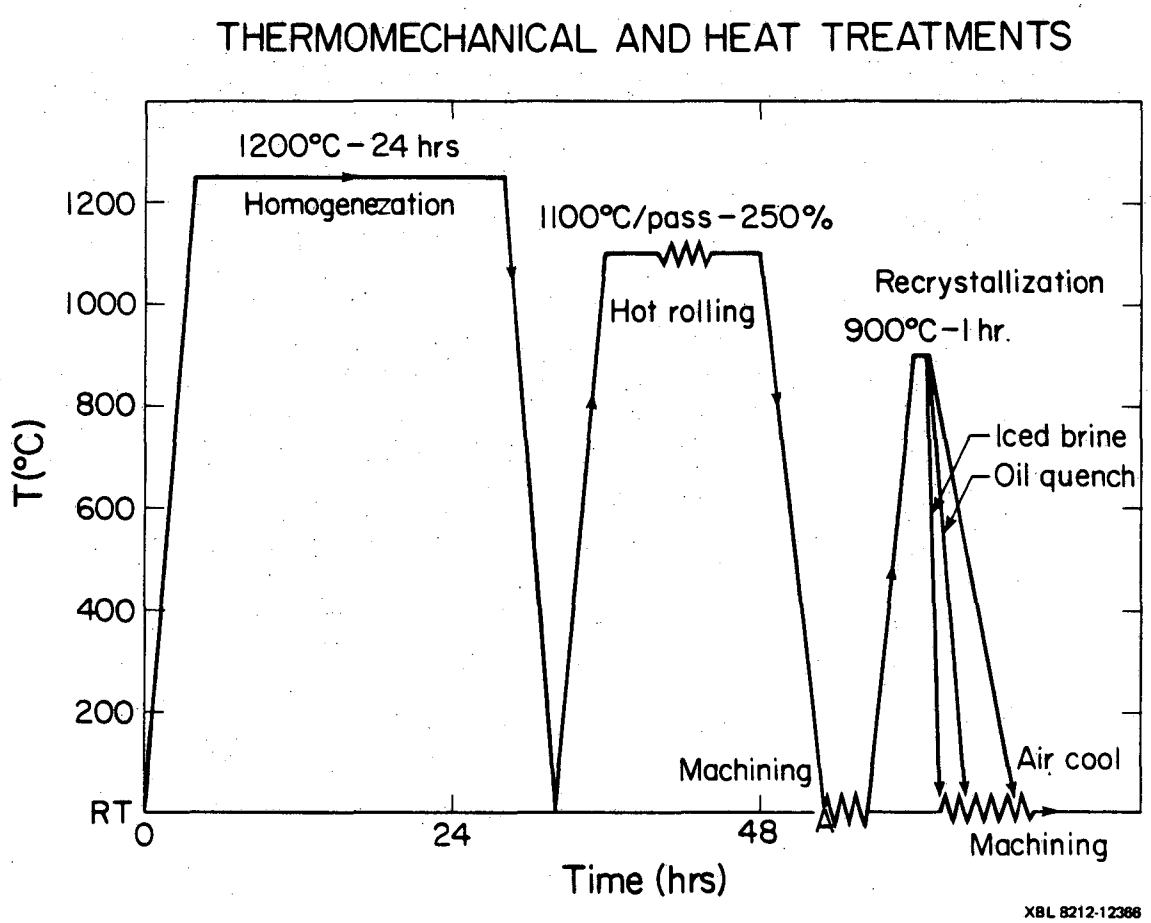
THERMOMECHANICAL AND HEAT TREATMENTS
1200°C – 24 hrs
Homogenezation
1100°C/pass – 250%
Hot rolling
Recrystallization
900°C – 1 hr.
Iced brine
Oil quench
Air cool
Machining
Machining
T(°C)
1200
1000
800
600
400
200
RT
0
24
48
Time (hrs)
XBL 8212-12366

Figure 1.

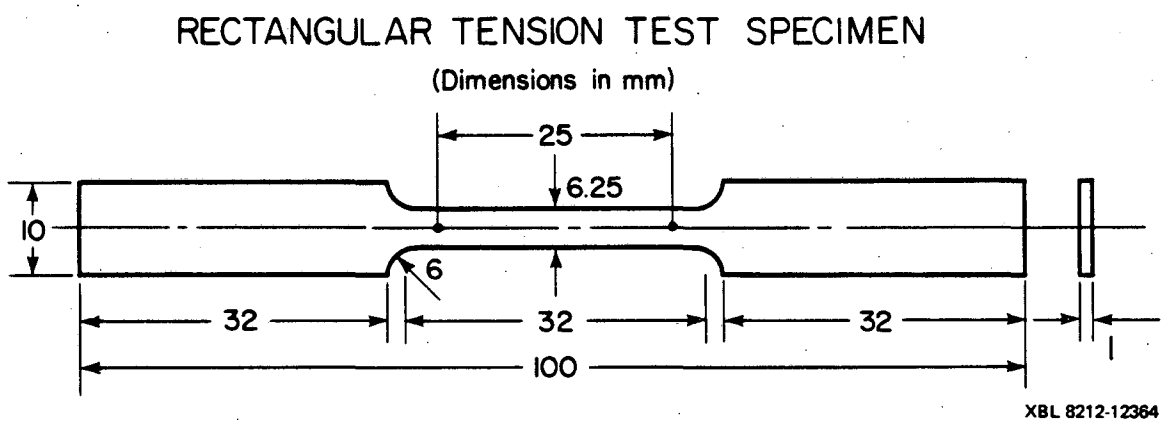
RECTANGULAR TENSION TEST SPECIMEN
(Dimensions in mm)
25
6.25
10
6
32
32
32
100
1
XBL 8212-12364

Figure 2.

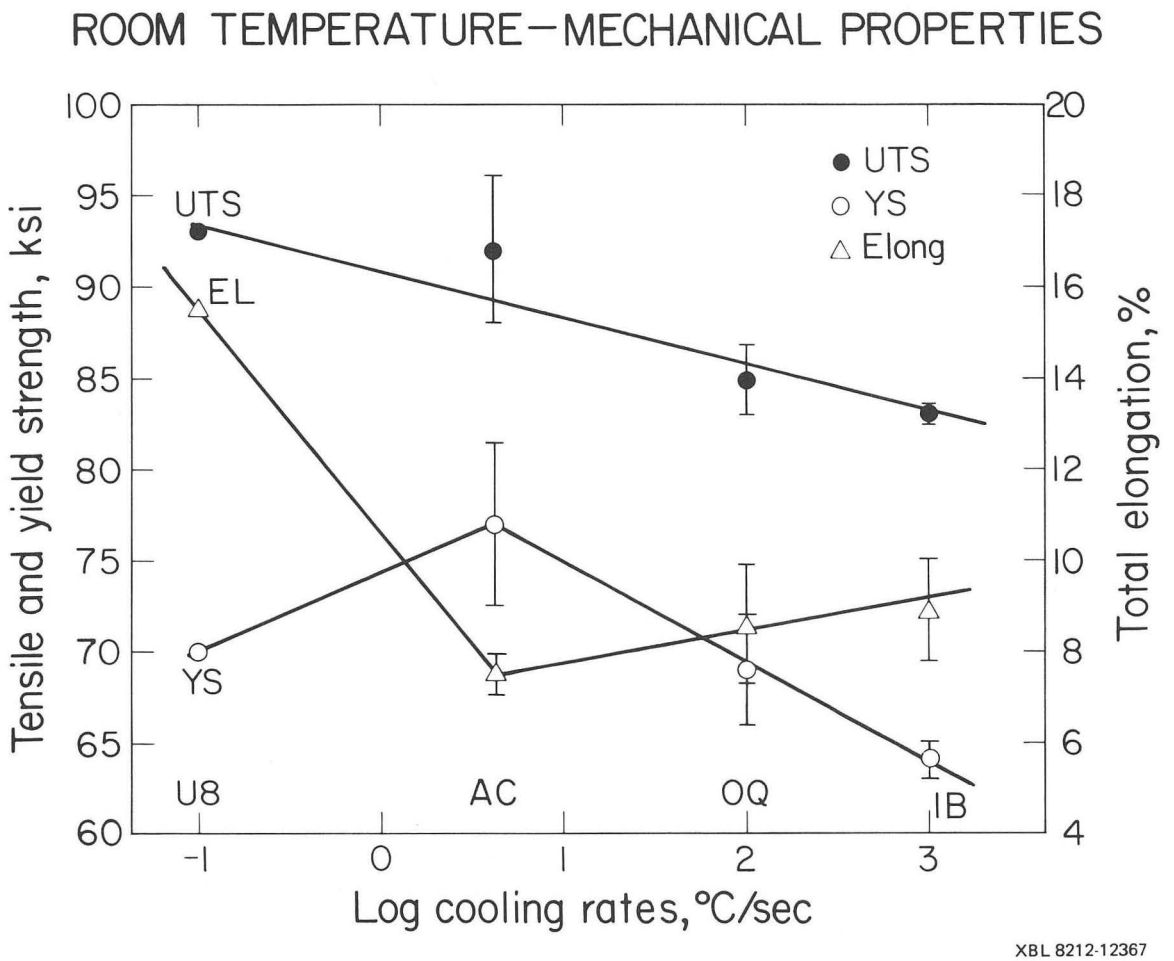
ROOM TEMPERATURE—MECHANICAL PROPERTIES
Tensile and yield strength, ksi
Total elongation, %
Log cooling rates, °C/sec
UTS
YS
Elong
EL
U8
AC
OQ
IB
100
95
90
85
80
75
70
65
60
20
18
16
14
12
10
8
6
4
-1
0
1
2
3
XBL 8212-12367

Figure 3.

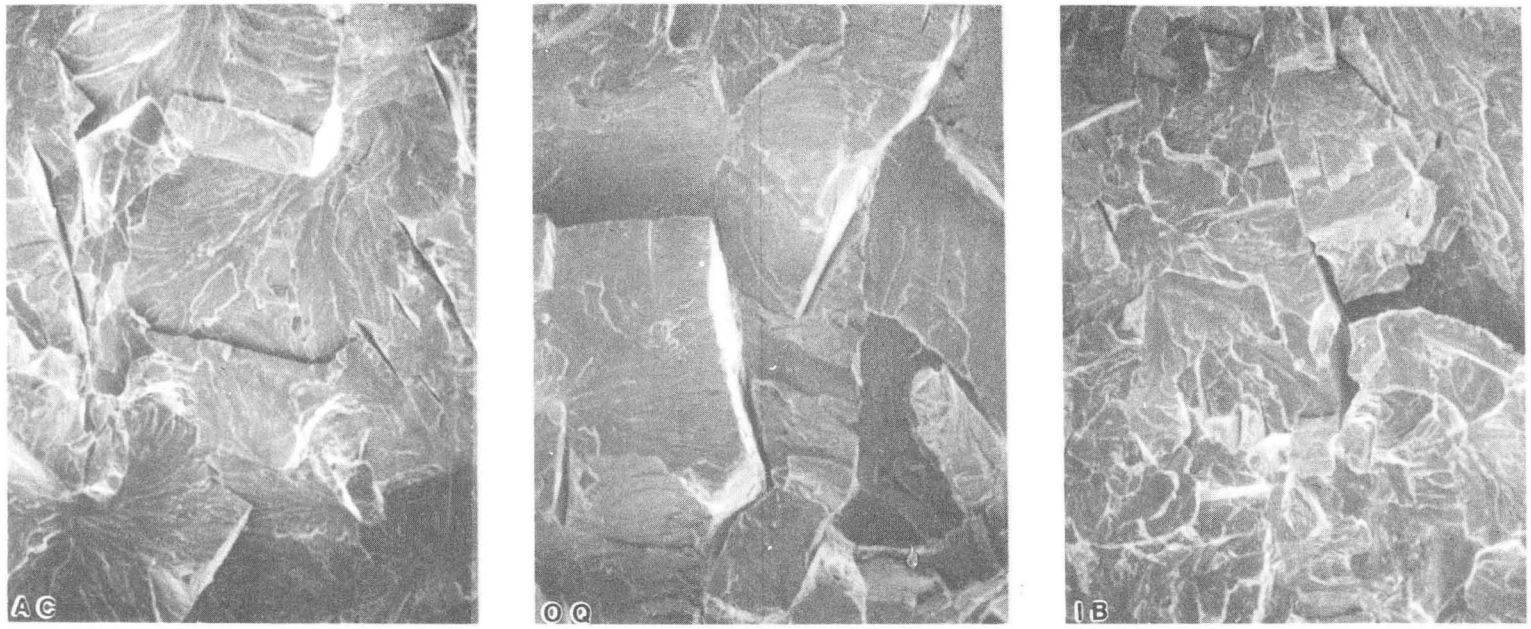

XBB 820-10828

100 μm

Figure 4.

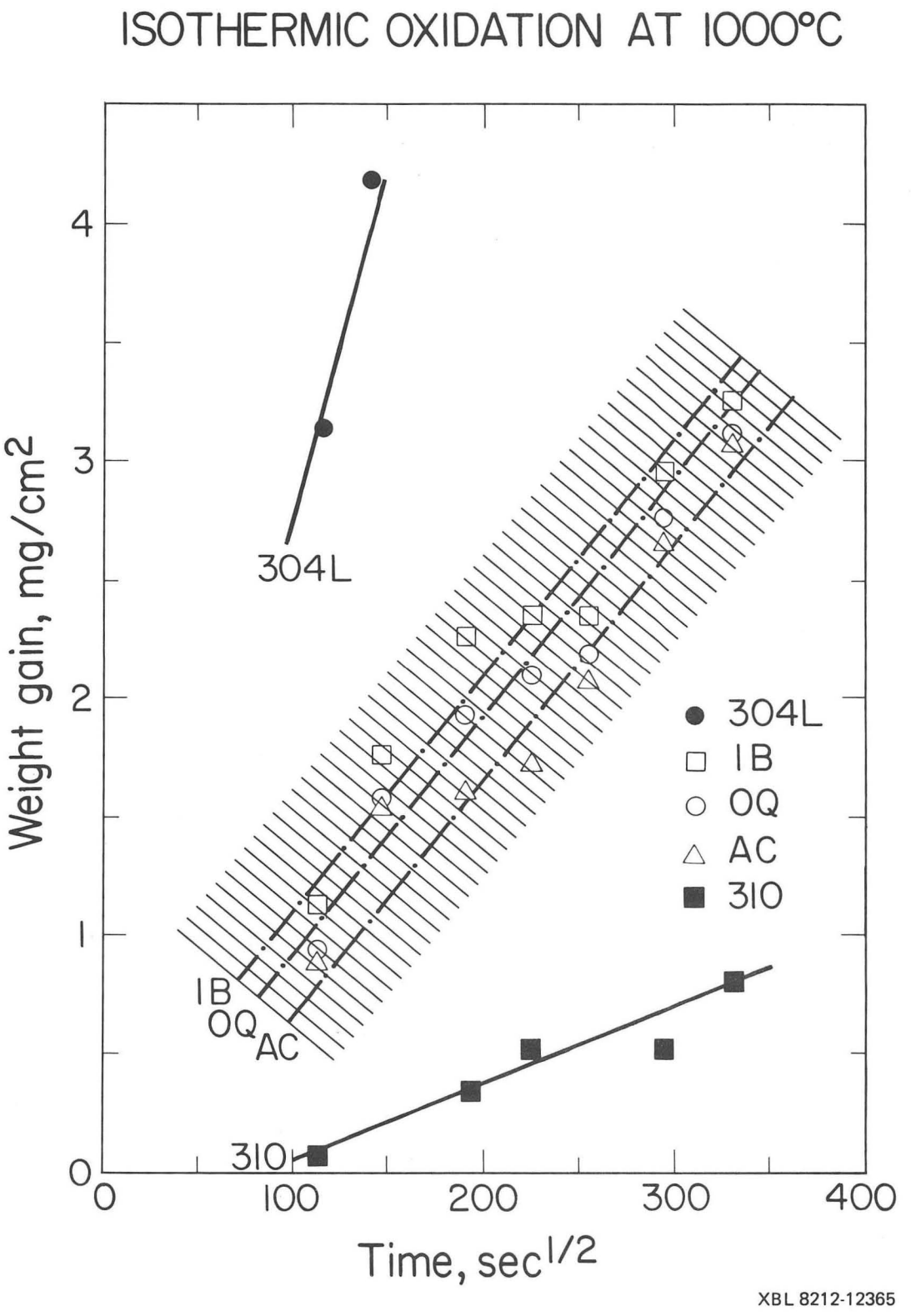
ISOTHERMIC OXIDATION AT 1000°C
Weight gain, mg/cm2
Time, sec1/2
0
1
2
3
4
0
100
200
300
400
304L
IB
OQ
AC
310
304L
IB
OQ
AC
310
XBL 8212-12365

Figure 5.

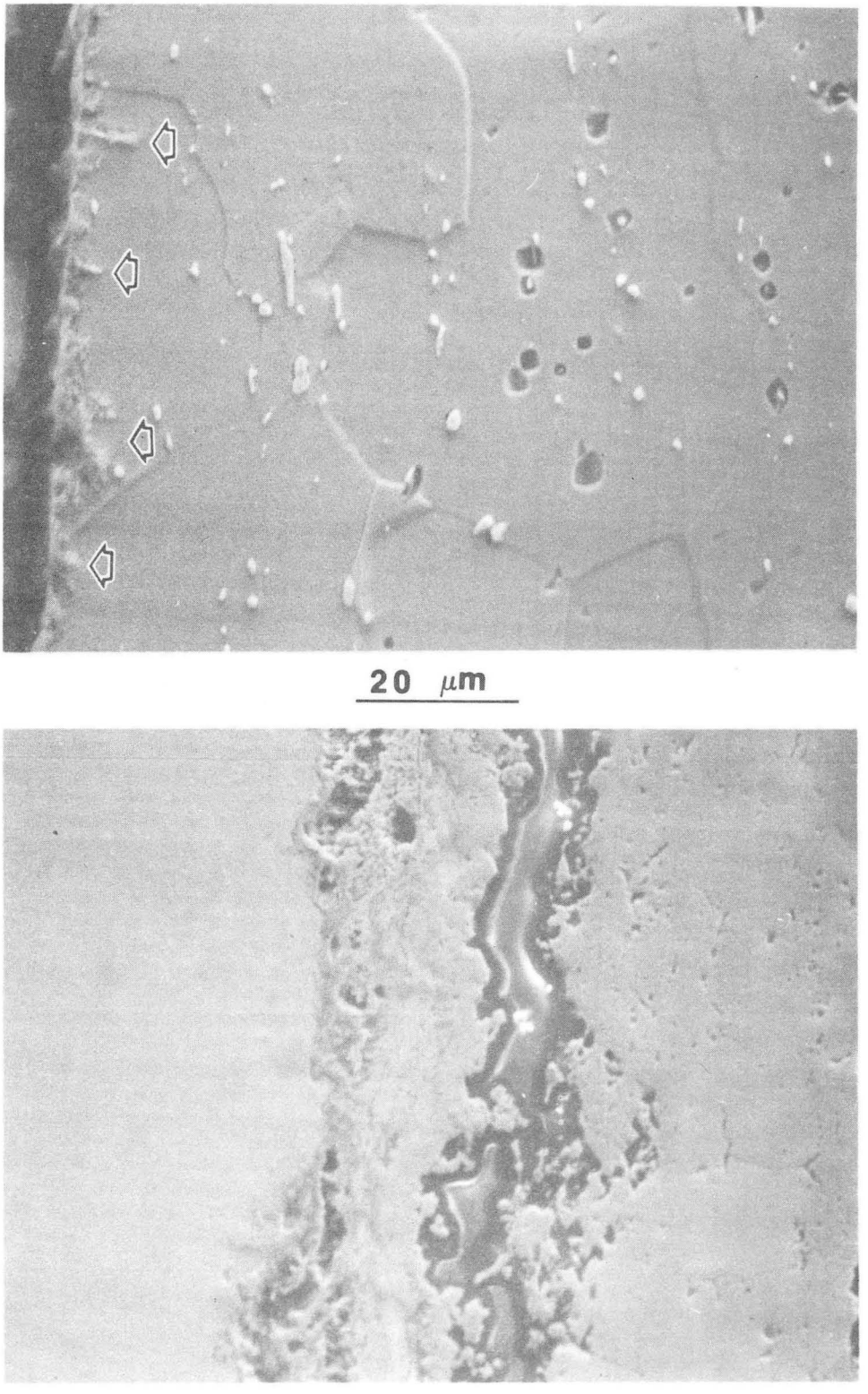

XBB 820-10829

Figure 6.

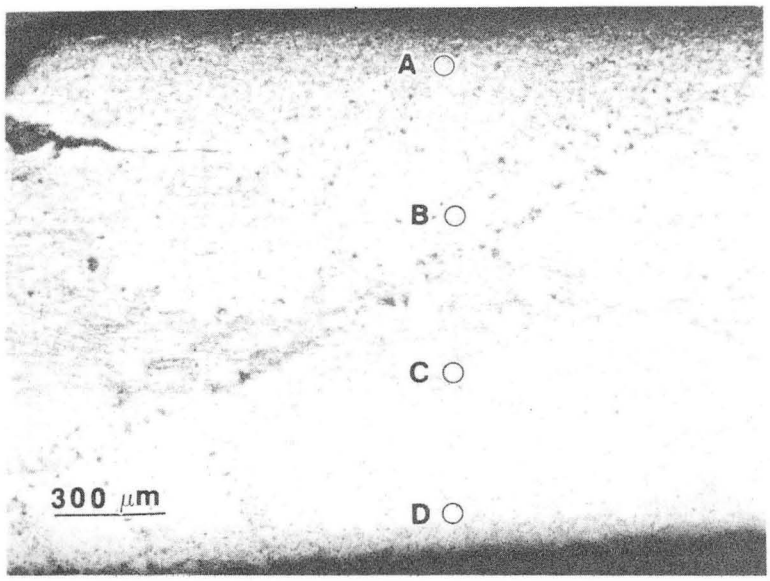

STANDARDLESS EDS ANALYSIS
(ZAF CORRECTIONS VIA MAGIC V)

	ELEMENT & LINE	WEIGHT PERCENT	ATOMIC PERCENT	PRECISION 2 SIGMA	K-RATIO	ITER
A	AL KA	9.33	16.74	0.17	0.0388	
	FE KA	93.03	80.64	0.37	0.9207	
	MO LA	5.12	2.58	0.24	0.0393	
	CE LA	0.11	0.04	0.15	0.0011	3
B	AL KA	8.98	16.19	0.20	0.0374	
	FE KA	92.93	81.00	0.37	0.9201	
	NB LA	0.06	0.03	0.21	0.0005	
	MO LA	5.47	2.77	0.28	0.0421	3
C	AL KA	7.87	14.48	0.19	0.0328	
	FE KA	91.87	81.71	0.37	0.9103	
	NB LA	0.24	0.13	0.26	0.0018	
	MO LA	7.11	3.68	0.30	0.0551	3
D	AL KA	6.12	11.62	0.18	0.0255	
	FE KA	91.34	83.71	0.37	0.9064	
	ZR LA	0.09	0.05	0.20	0.0007	
	MO LA	8.65	4.62	0.29	0.0675	3

XBB 820-10835

Figure 7.

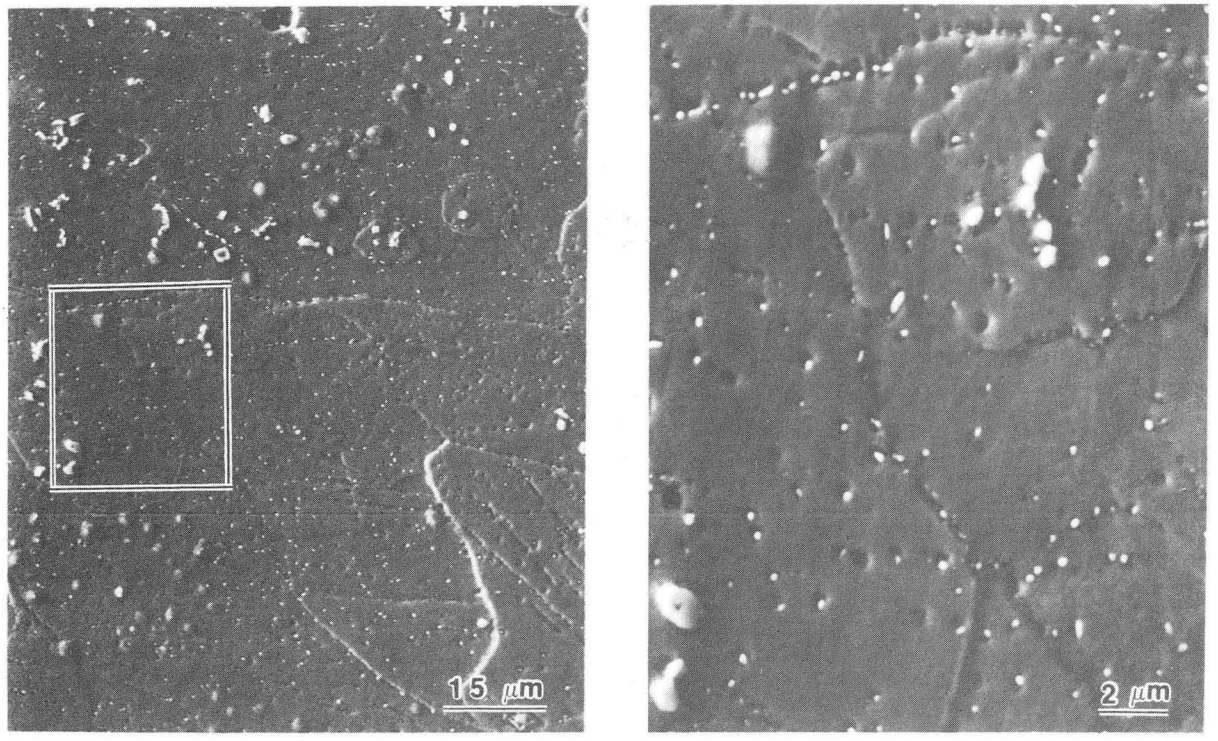

XBB 820-10832

Figure 8.

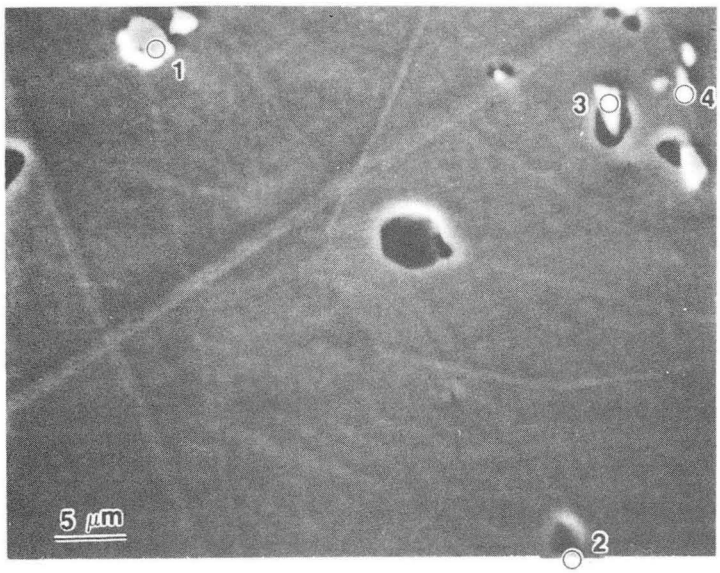

STANDARDLESS EDS ANALYSIS
(ZAF CORRECTIONS VIA MAGIC V)

	ELEMENT & LINE	WEIGHT PERCENT	ATOMIC PERCENT	PRECISION 2 SIGMA	K-RATIO	ITER
1	AL KA	8.13	21.25	0.31	0.0282	
	FE KA	13.85	17.49	0.28	0.1288	
	ZR LA	28.96	22.39	0.70	0.1913	
	NB LA	0.86	0.65	0.71	0.0061	
	MO LA	6.66	4.90	0.59	0.0425	
	CE LA	66.21	33.32	0.66	0.6032	4
2	AL KA	5.42	10.37	0.23	0.0201	
	FE KA	85.85	79.27	0.34	0.8490	
	ZR LA	12.98	7.34	0.47	0.0908	
	NB LA	0.54	0.30	0.45	0.0040	
	MO LA	5.04	2.71	0.38	0.0356	
	CE LA	0.04	0.02	0.09	0.0004	3
3	AL KA	2.53	5.44	0.19	0.0110	
	FE KA	60.23	62.56	0.36	0.5943	
	ZR LA	45.18	28.73	0.72	0.3550	
	NB LA	3.05	1.90	0.73	0.0253	
	MO LA	2.21	1.34	0.60	0.0140	
	CE LA	0.05	0.02	0.12	0.0005	3
4	AL KA	0.42	1.21	0.14	0.0024	
	FE KA	15.31	21.44	0.24	0.1508	
	ZR LA	82.96	71.11	0.83	0.7749	
	NB LA	7.42	6.24	0.93	0.0717	
	MO LB	0.00	0.00	-0.00	0.0000	4

XBB 820-10836

Figure 9.

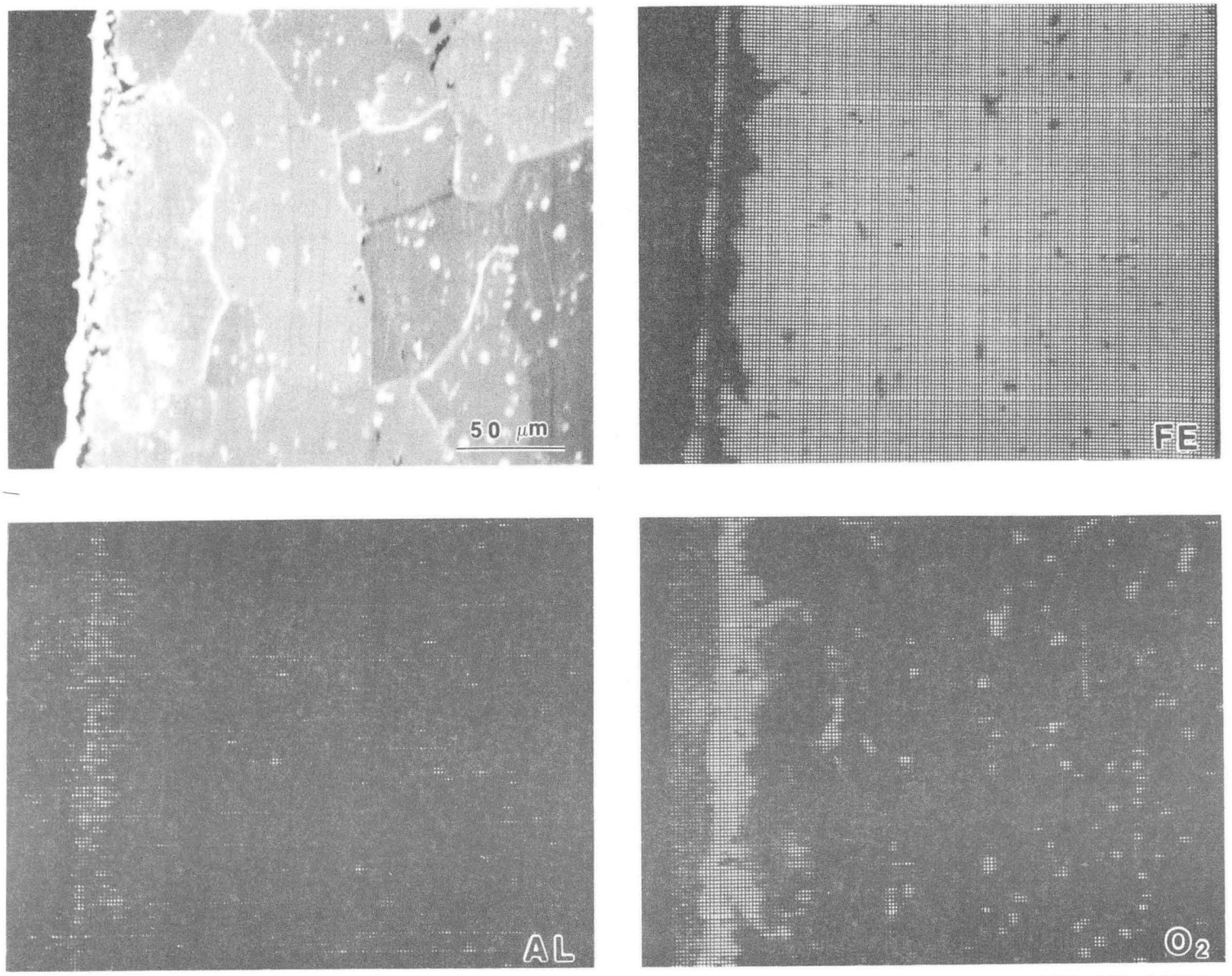

XBB 820-10830

Figure 10(a)

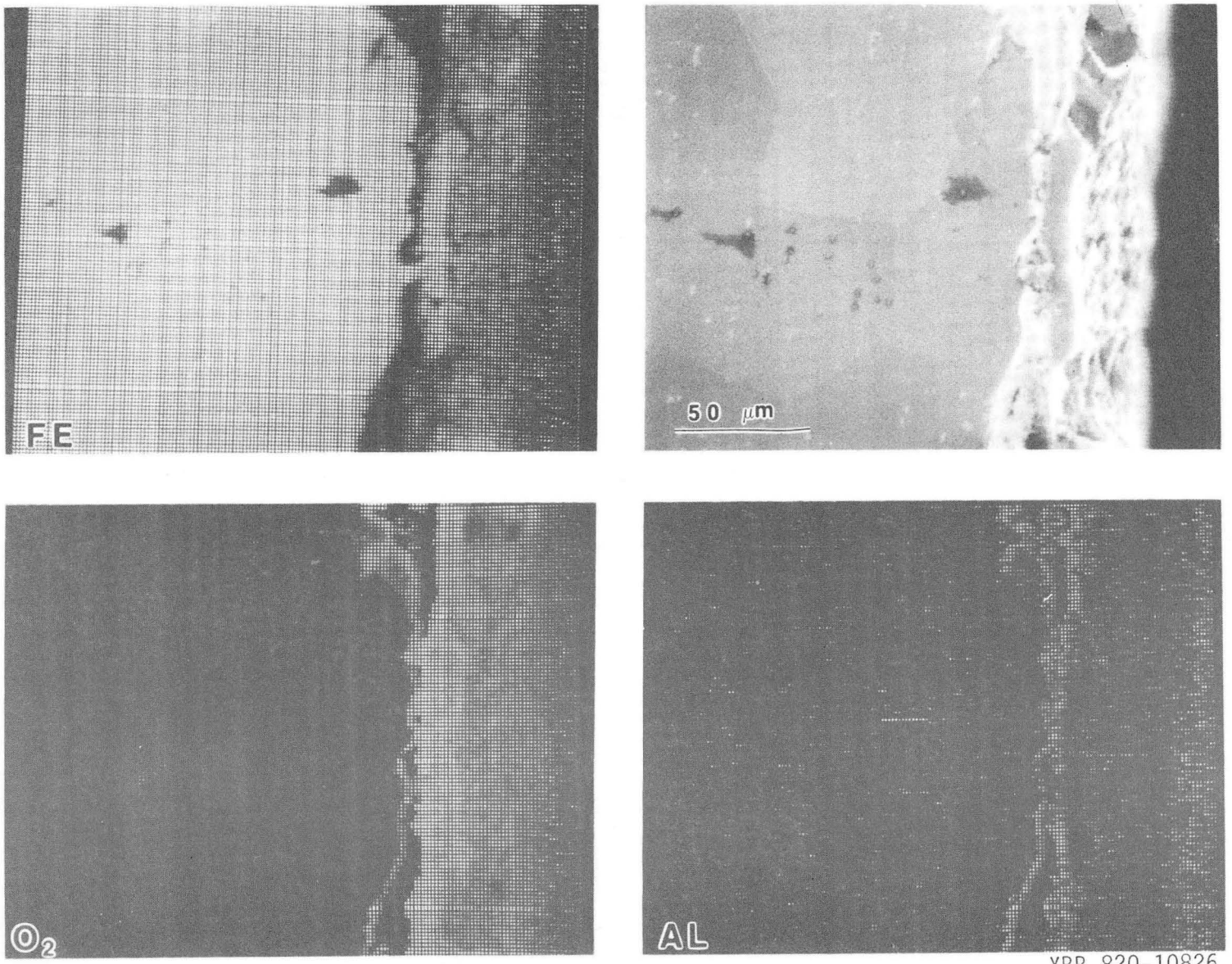

XBB 820-10826

Figure 10(b)

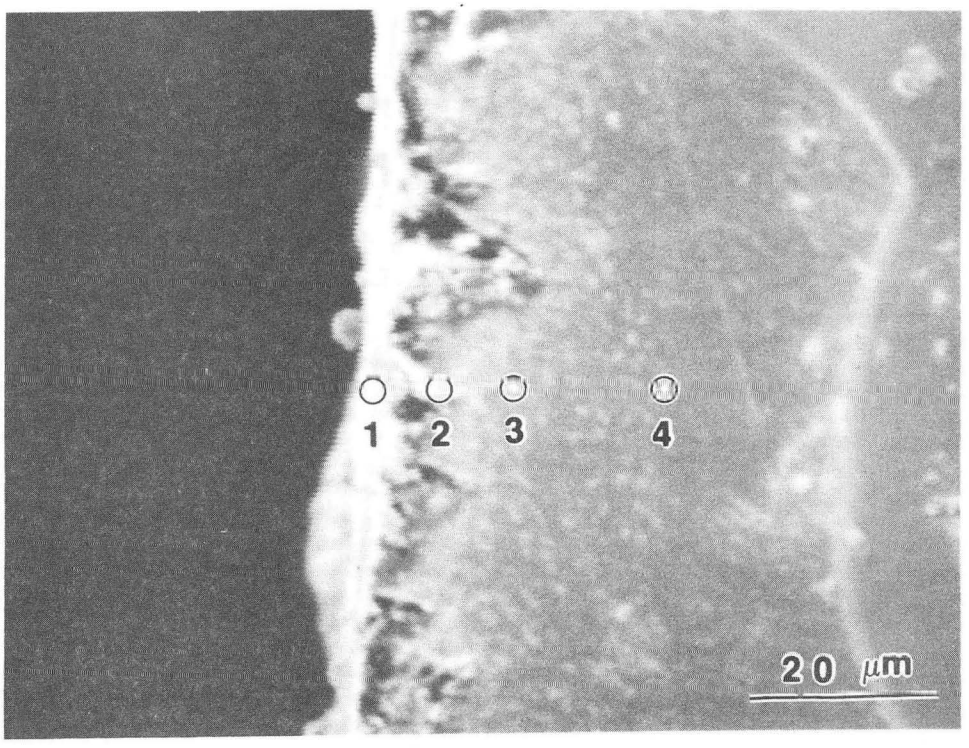

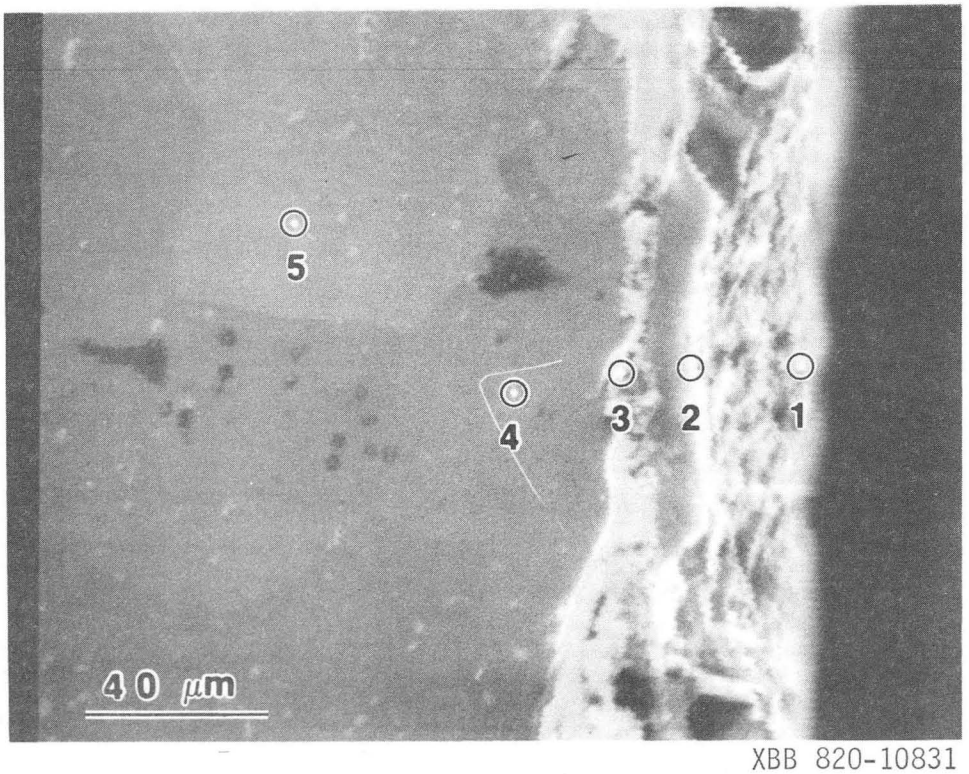

XBB 820-10831

Figure 11(a)

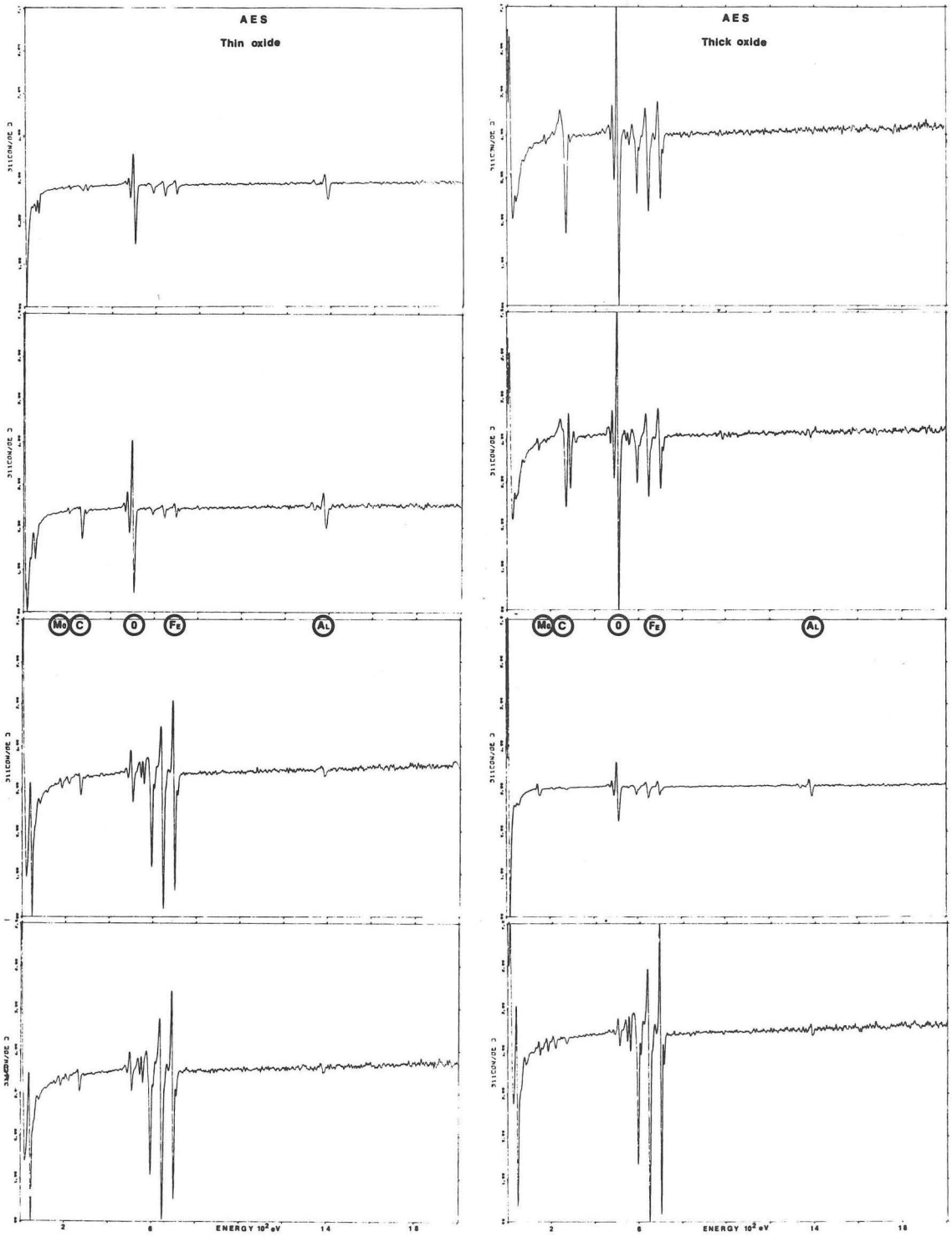

XBL 8212-12274

Figure 11(b)

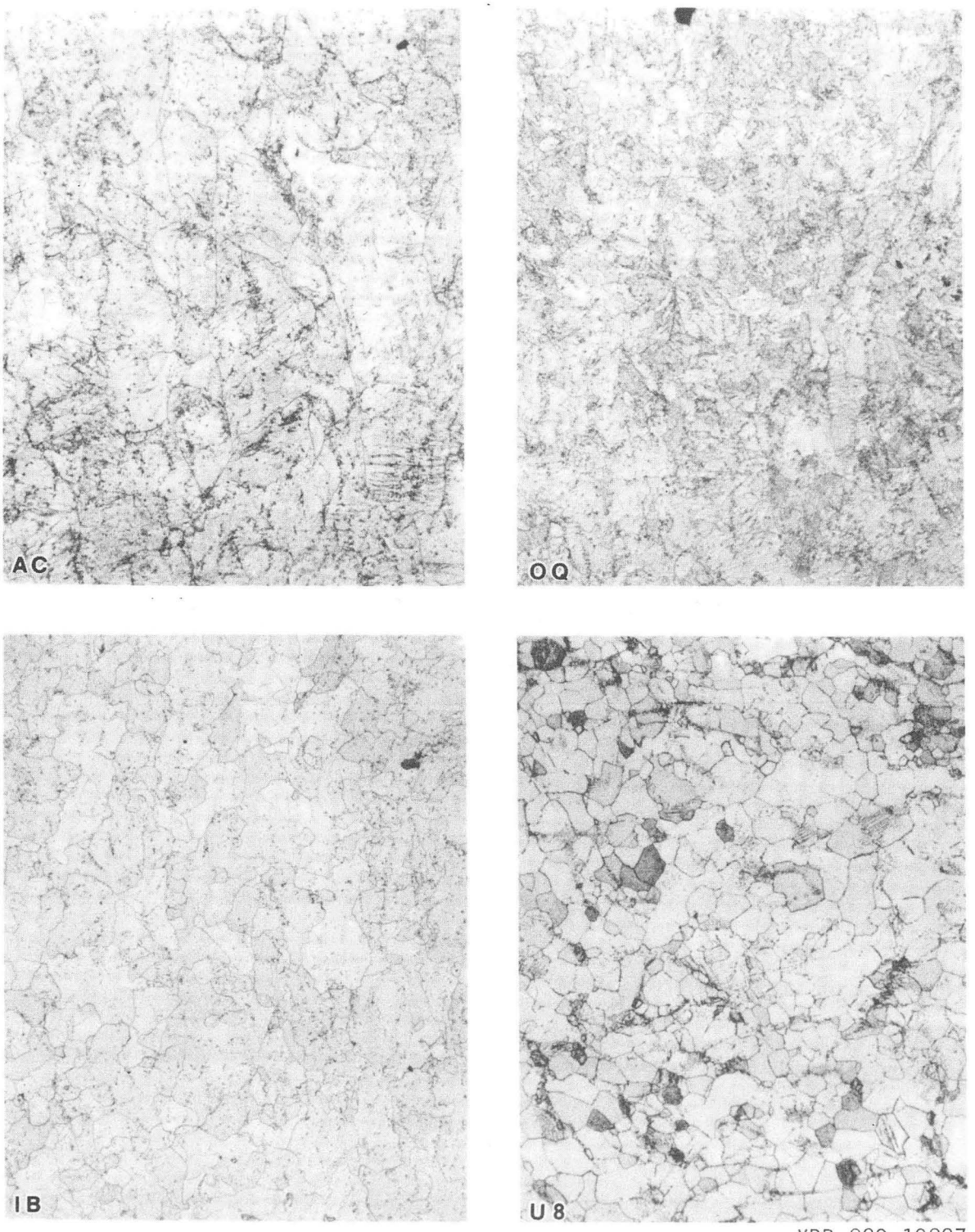

XBB 820-10827

250 μm

Figure 12.

XBB 820-10824

Figure 13.

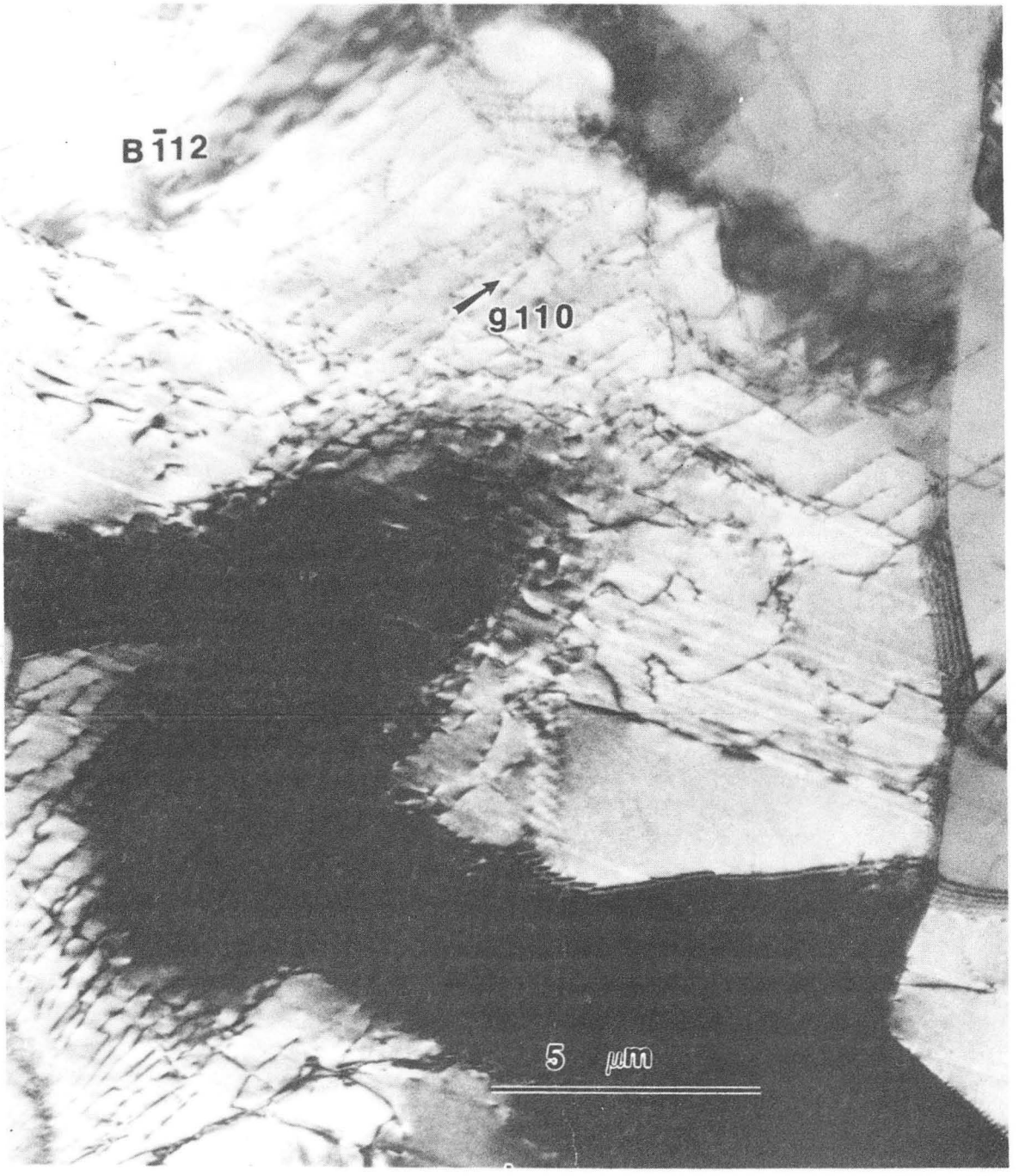

XBB 820-10825

Figure 14.

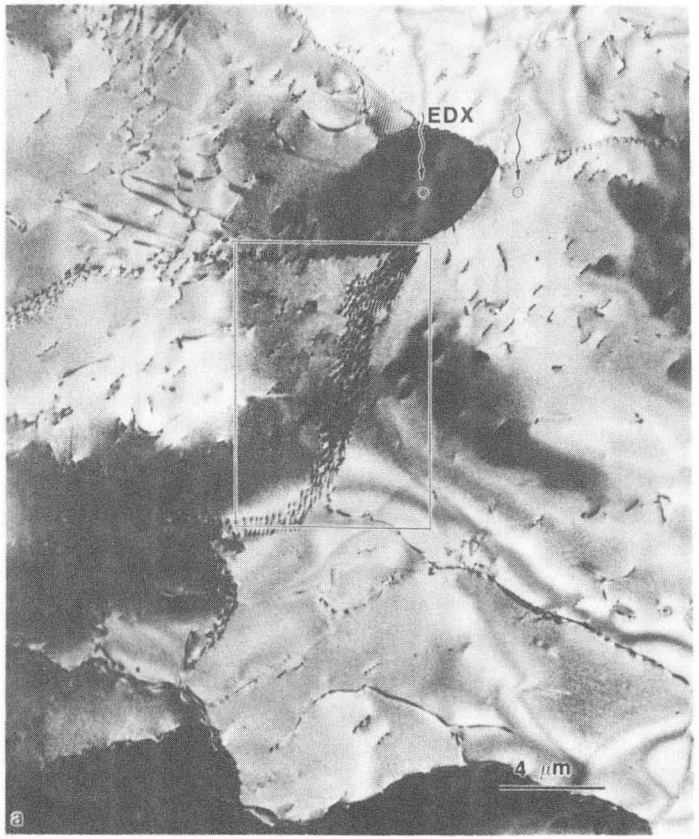

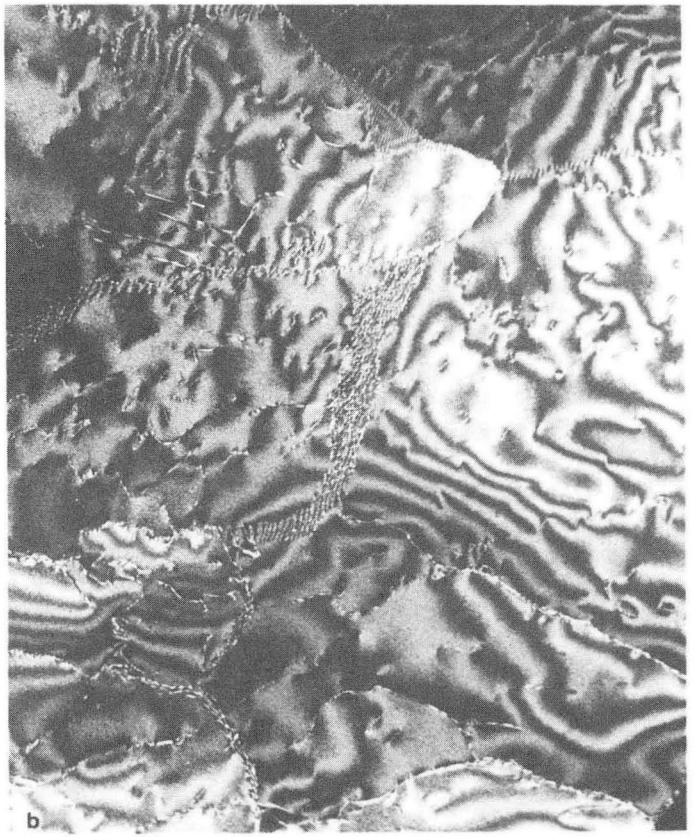

XBB 820-10821

Figure 15.

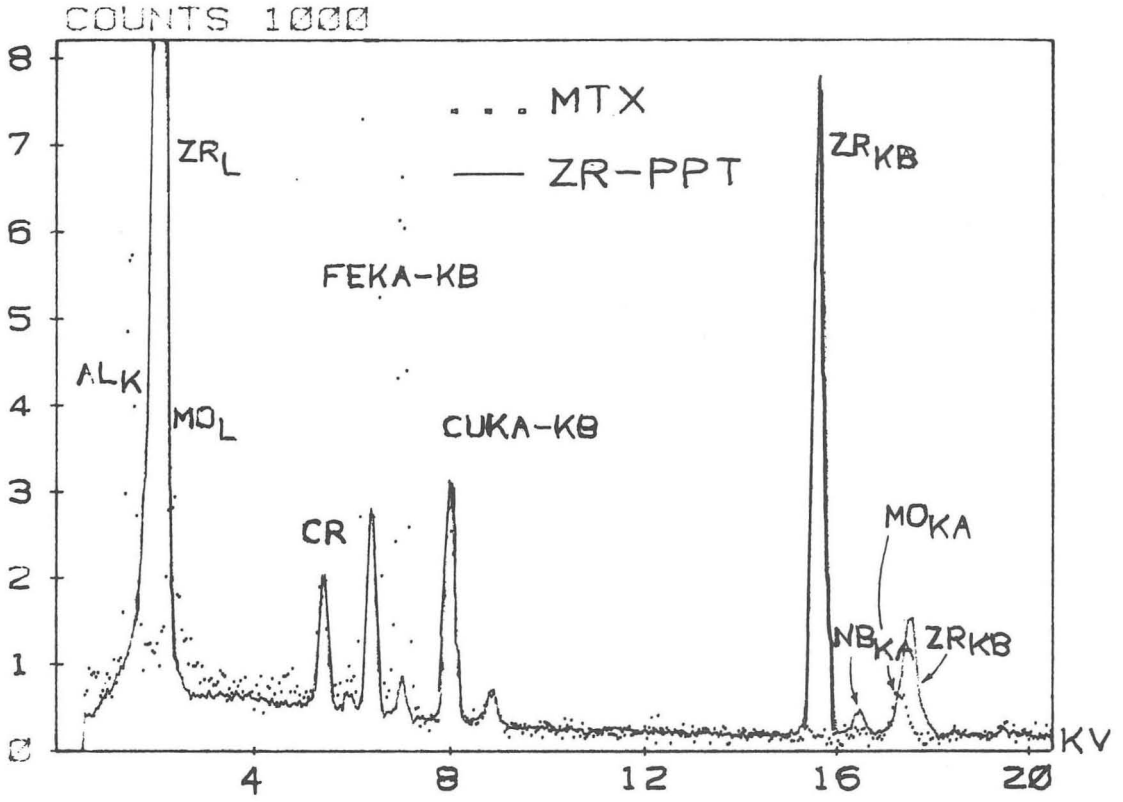

c

XBL 8212-12261

Figure 15. (cont.)

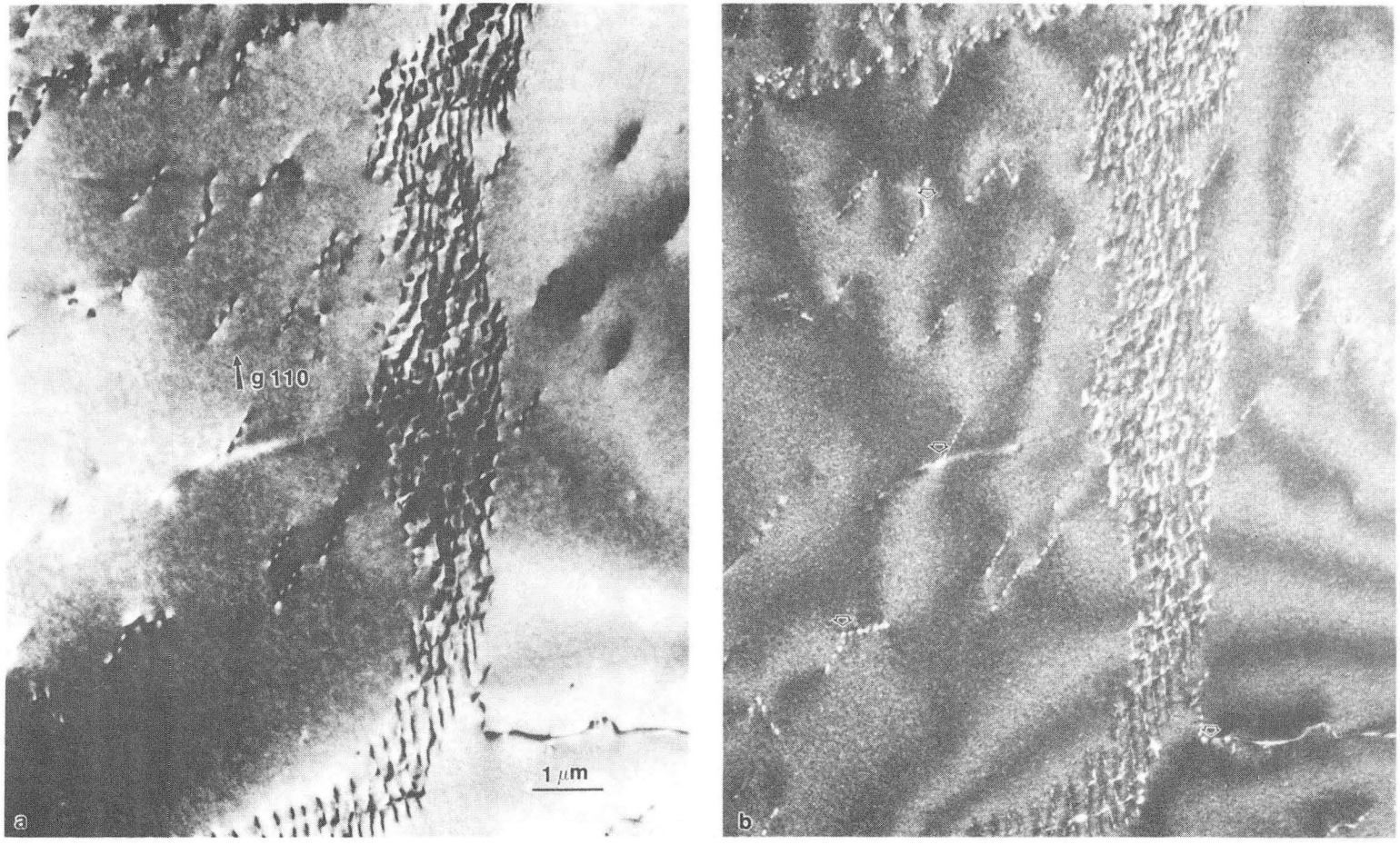

XBB 820-10820

Figure 16.

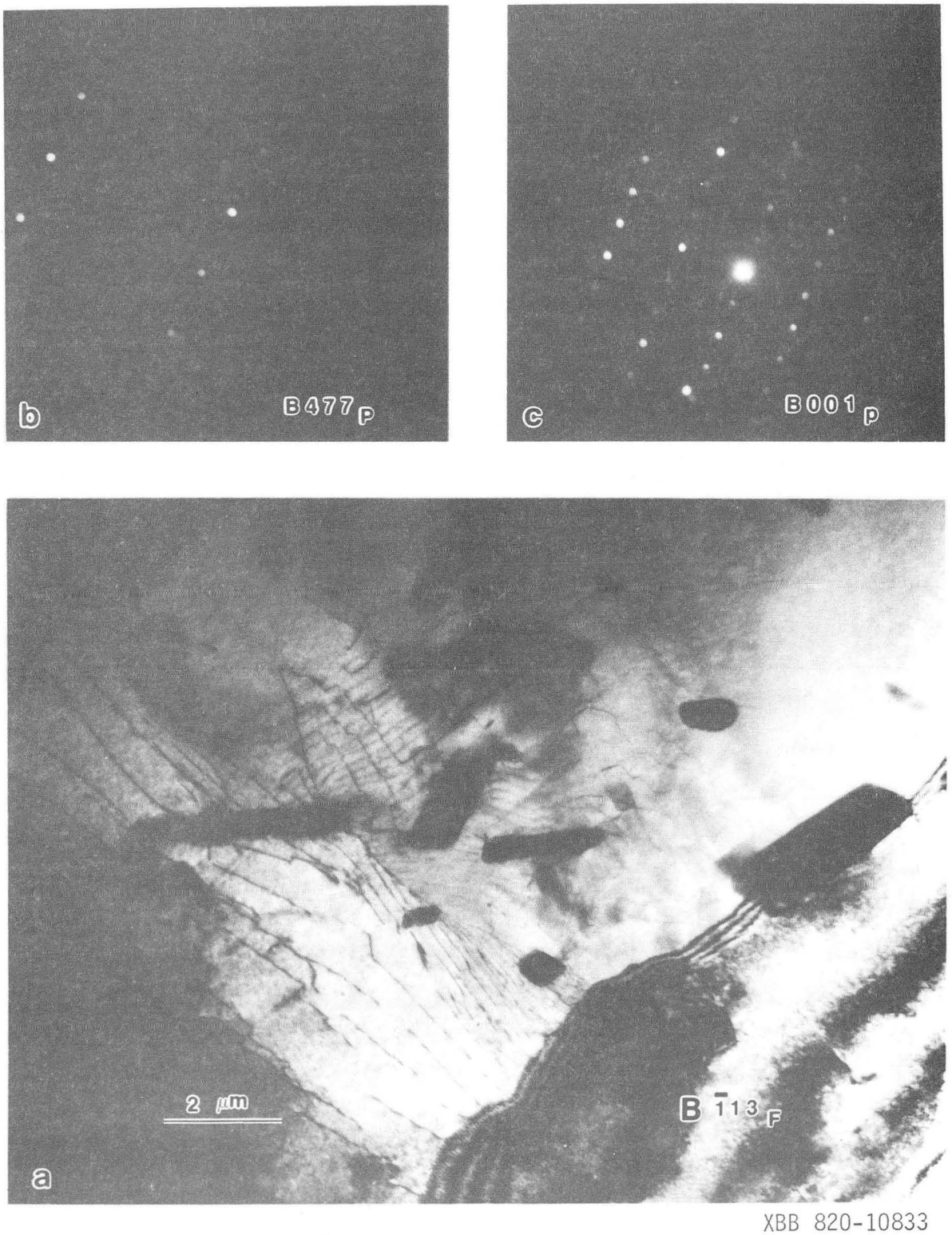

XBB 820-10833

Figure 17.

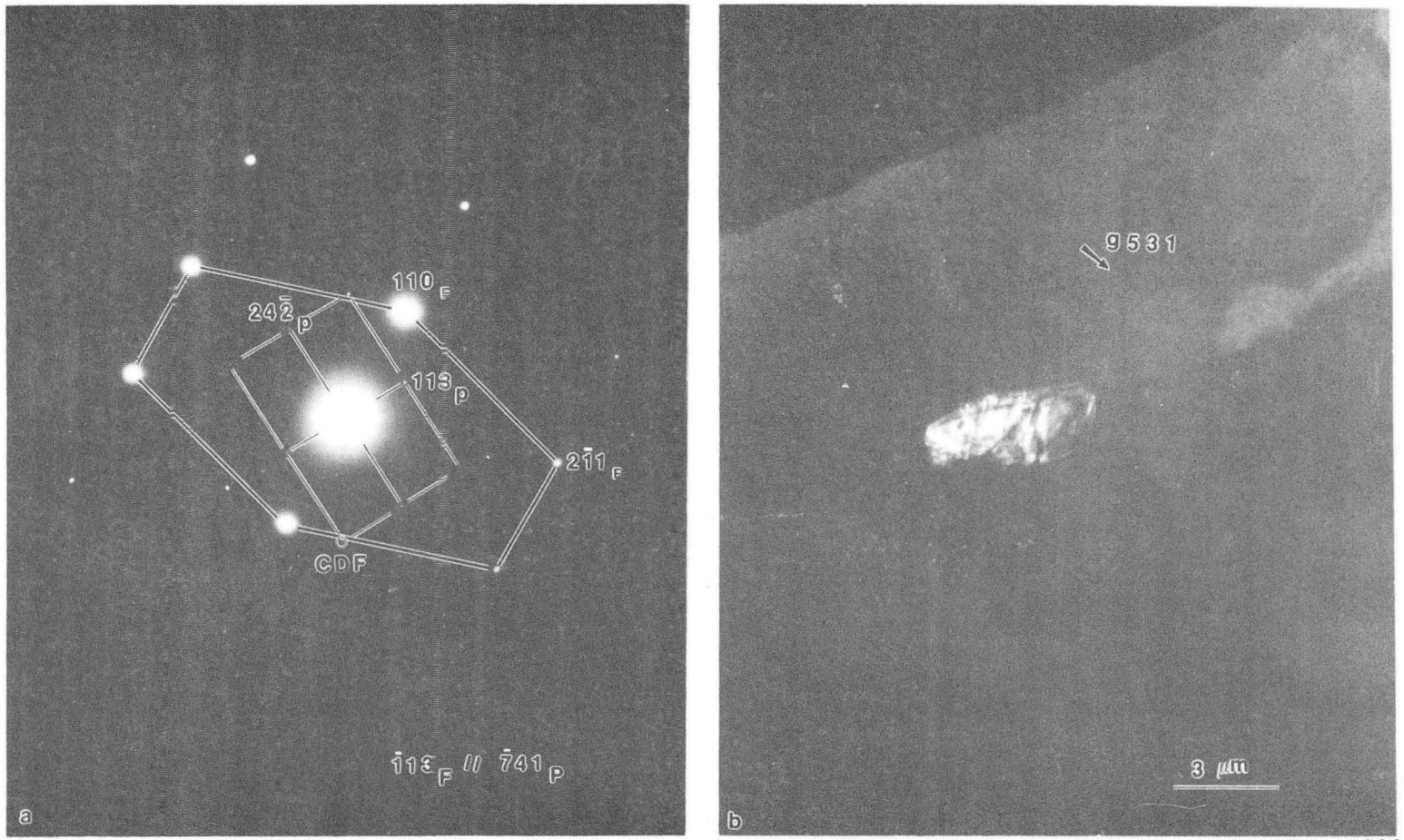

XBB 820-10822

Figure 18.

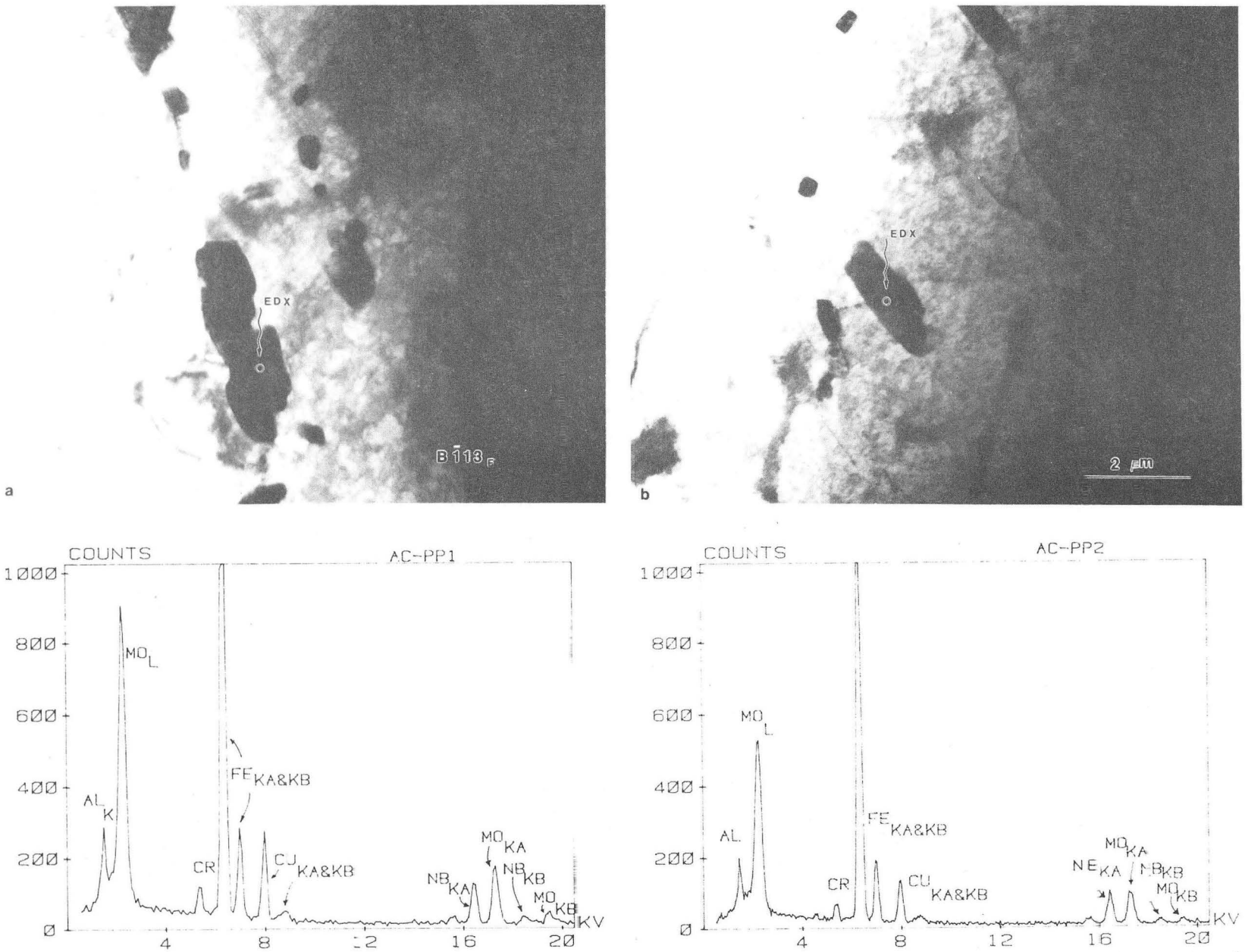

Figure 19.

XBB 320-10817

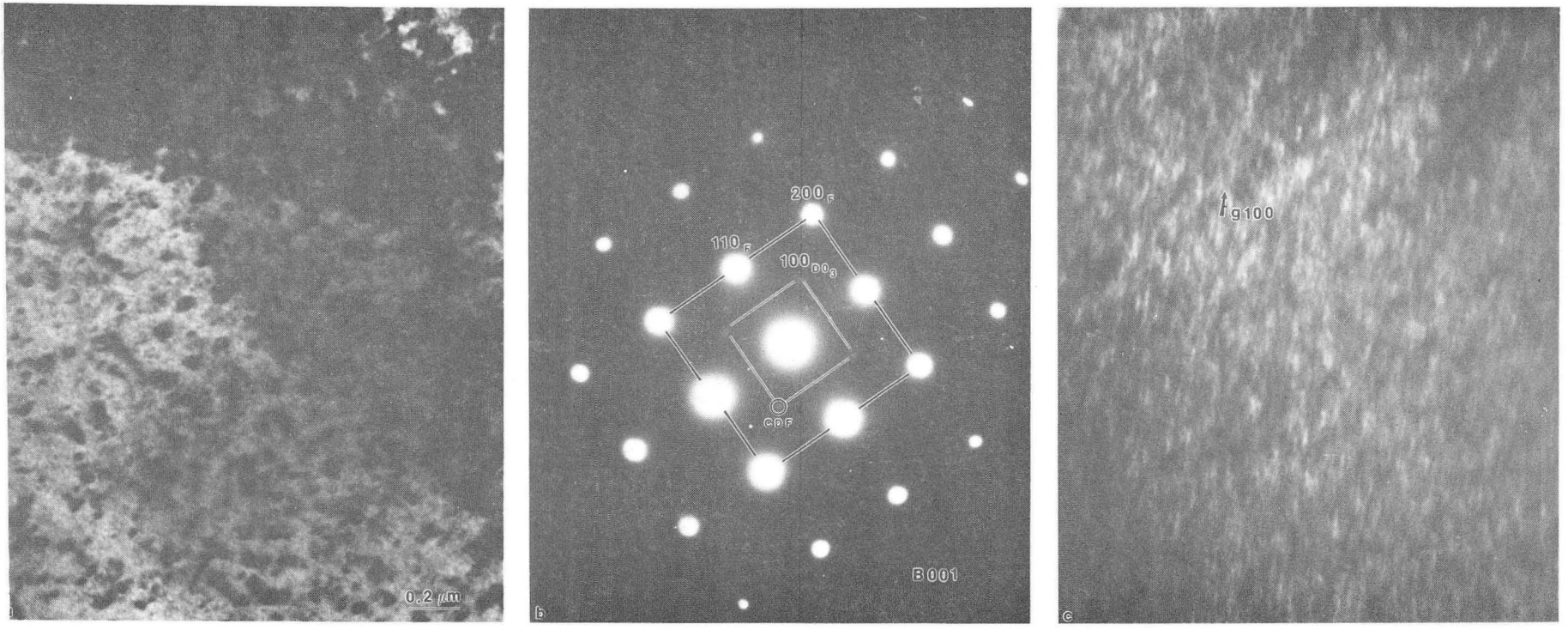

XBB 820-10819

Figure 20.

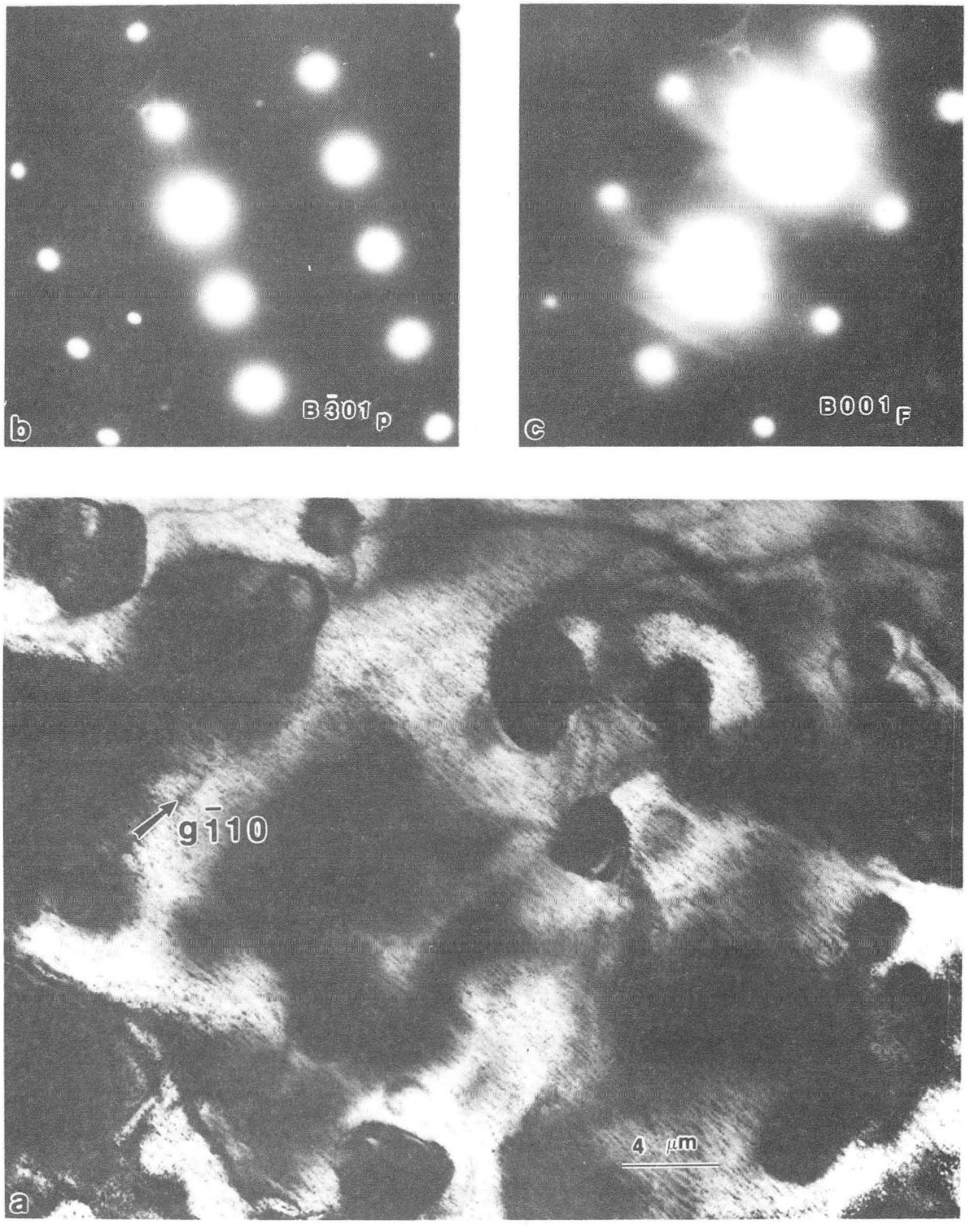

XBB 820-10834

Figure 21.

EDX
5 μm

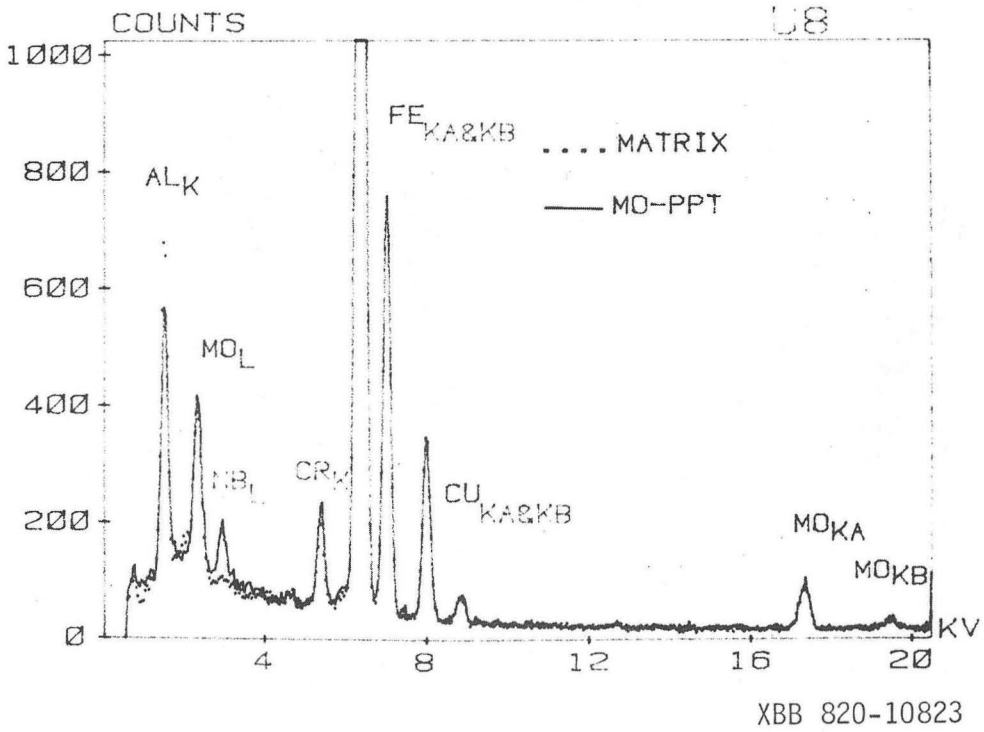
COUNTS
U8
1000
800
600
400
200
0
AL K
MO L
NB L
CR K
FE KA&KB
CU KA&KB
MO KA
MO KB
.... MATRIX
—— MO-PPT
4
8
12
16
20
KV
XBB 820-10823

Figure 22.

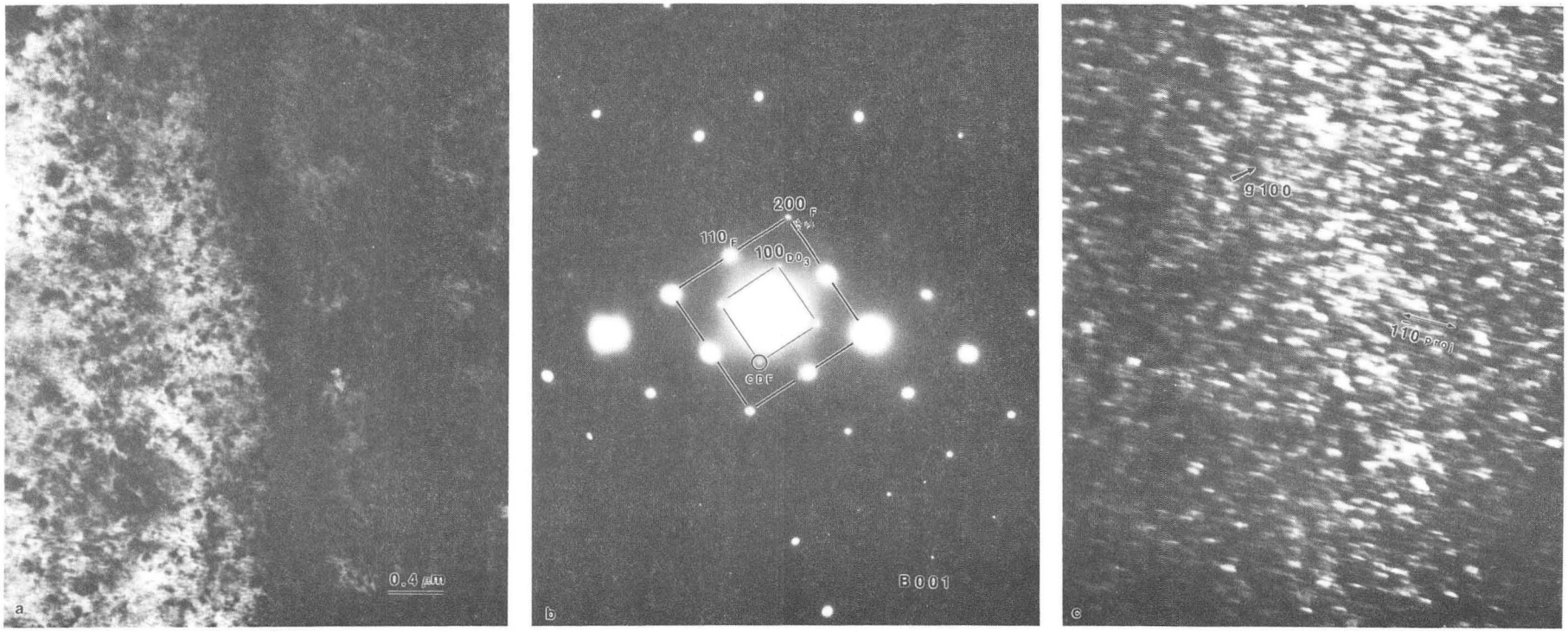

XBB 820-10818

Figure 23.

This report was done with support from the Department of Energy. Any conclusions or opinions expressed in this report represent solely those of the author(s) and not necessarily those of The Regents of the University of California, the Lawrence Berkeley Laboratory or the Department of Energy.

Reference to a company or product name does not imply approval or recommendation of the product by the University of California or the U.S. Department of Energy to the exclusion of others that may be suitable.

TECHNICAL INFORMATION DEPARTMENT
LAWRENCE BERKELEY LABORATORY
UNIVERSITY OF CALIFORNIA
BERKELEY, CALIFORNIA 94720